RMetS

Royal Meteorological Society

The dynamics of intensification in a Hurricane Weather Research and Forecasting simulation of Hurricane *Earl* (2010)

Roger K. Smith,[a] Jun A. Zhang[b]* and Michael T. Montgomery[c]

[a]*Meteorological Institute, Ludwig-Maximilians University of Munich, Germany*
[b]*NOAA/AOML Hurricane Research Division with University of Miami/CIMAS, Miami, FL, USA*
[c]*Department of Meteorology, Naval Postgraduate School, Monterey, CA, USA*

*Correspondence to: J. A. Zhang, NOAA Hurricane Research Division, 4301 Rickenbacker Causeway, Miami, FL, 33149, USA.
E-mail: jun.zhang@noaa.gov*

We use a high-resolution numerical simulation of Atlantic Hurricane *Earl* (2010) to increase our understanding of *Earl*'s intensification in relatively strong vertical shear in the context of a recent paradigm for tropical cyclone intensification. The integrity of the simulation is judged by comparing analyses thereof with those of the unprecedented observational data gathered in *Earl*. Consistent with the classical view of spin-up, the amplification of the tangential wind field above the boundary layer is found to occur as the absolute angular momentum surfaces are drawn inwards by the aggregate heating of the rotating convective clouds in the interior of the vortex. In addition to this classical pathway, spin-up occurs within the inner-core boundary layer, where the maximum tangential winds occur. The latter is another element of the new paradigm.

Despite the detrimental influence of the shear on the vortex alignment and in depressing the pseudo-equivalent potential temperature outside the developing eyewall, the combined eddy processes associated with the vortical plume structures in and around the developing eyewall region are shown to contribute to an enhanced overturning circulation and an intensifying storm. These eddy processes are distinctly agradient effects that are not features of the classical spin-up mechanism. It remains to be understood how the rotating convective updraughts combine to produce the diagnosed structures of the eddy terms themselves and how vortex Rossby waves and other eddies contribute to the alignment of the vortex during intensification.

Key Words: hurricanes; typhoons; classical spin-up mechanism; boundary-layer spin-up mechanism; eddy dynamics; vertical shear

Received 21 October 2015; Revised 11 August 2016; Accepted 7 September 2016; Published online in Wiley Online Library 25 November 2016

1. Introduction

The three (and sometimes four) aircraft that flew in Atlantic Hurricane *Earl* (2010) collected an unprecedented amount of observational data (Montgomery *et al.*, 2014; Rogers *et al.*, 2015). Indeed, this hurricane is arguably the most thoroughly documented storm undergoing rapid intensification (RI) to date. Given this comprehensive data set and the computational resources now available, it is imperative that efforts be made to understand the dynamics of *Earl*'s intensification. Here we use these observations combined with a state-of-the-art hurricane forecast model to appraise elements of a new paradigm for tropical-cyclone intensification articulated in a series of articles by Nguyen *et al.* (2008), Bui *et al.* (2009), Montgomery *et al.* (2009, 2015), Smith *et al.* (2009) and summarized by Montgomery and Smith (2014). This new paradigm is needed because it provides

a framework for understanding features of the intensification process, which earlier theories are unable to capture (Montgomery *et al.* 2015, p. 2).

One feature of the new intensification paradigm is its recognition of the intrinsic asymmetric nature of the intensification process involving the collective action of rotating deep convective structures. Another feature is the fact that, in an azimuthal-average view, the spin-up of the maximum tangential wind speed occurs in the frictional boundary, which at first sight is surprising and counter-intuitive. This recognition of the subtle dynamical role of the boundary layer has had ramifications in understanding the dependence of spin-up rate on latitude (Smith *et al.*, 2015) and the progressive growth in size of both the eyewall radius and the radius of gale force winds (Kilroy *et al.*, 2015). A further feature is the positive contribution of eddy processes to vortex spin-up demonstrated in Persing *et al.* (2013), one that contrasts

with previous assumptions and speculation of the down-gradient action of asymmetric motions that would lead to spin-down.

In the classical axisymmetric view of spin-up, it is supposed that deep convection in a localized region will induce a secondary (or overturning) circulation with inflow in the lower troposphere and outflow in the upper troposphere (e.g. Charney and Eliassen, 1964; Ooyama, 1969, 1982; Carrier, 1971). This inflow converges absolute angular momentum (M) surfaces above the boundary layer, where, to a first approximation, M is materially conserved. The quantity M is defined in terms of the azimuthally-averaged tangential velocity component $\langle v \rangle$ by the formula $M = r \langle v \rangle + \frac{1}{2} f r^2$, where r is the radius from the circulation centre and f is the Coriolis parameter, normally assumed constant. Because the flow above the boundary layer is close to gradient wind balance, the radial velocity component there is weak compared with the tangential component.

By far the largest inflow velocities occur in a shallow boundary layer on the order of 1 km deep. There, gradient wind balance is broken because of the frictional torque acting on the tangential wind, which reduces the Coriolis and centrifugal forces. However, the radially inward pressure gradient remains approximately the same as that at the top of the layer, leaving an inward-directed (agradient) force that drives the boundary-layer inflow (e.g. Smith, 1968). Although absolute angular momentum is not conserved in the boundary layer, if air parcels converging in this layer can reach small radii without losing too much absolute angular momentum then it is possible that larger tangential winds can be achieved in the boundary layer than in the free atmosphere (see e.g. Montgomery and Smith, 2014 and references therein).

As a start to building an understanding of *Earl*'s intensification, Montgomery *et al.* (2014) examined dynamical and thermodynamical aspects of the storm during a four-day period in which it underwent an episode of RI, maturity, secondary eyewall replacement, re-intensification and early decline. An analysis of these observations was used to appraise elements of the new paradigm. Montgomery *et al.* (2014) showed that the data gathered in *Earl* did, indeed, support the two processes of spin-up. In particular, they showed that the absolute angular momentum surfaces moved progressively inwards over a deep layer as *Earl* intensified and that, during spin-up and maturity, the maximum tangential wind speed occurred within the layer of strong boundary-layer inflow. Further, the tangential winds near the radius of maximum wind in the boundary layer were persistently and significantly supergradient, except very near the surface, where they became subgradient. The findings complemented a recent observational study by Sanger *et al.* (2014), which provided support also for the revised model for tropical cyclone intensification.

The rapid intensification of *Earl* took place in an environment of relatively strong vertical shear, an aspect that was not touched upon in Montgomery *et al.* (2014) and one that remains challenging, even using the outstanding set of observations by those authors. A useful review of research on hurricane development in vertical shear, as well as the results of some new numerical experiments, is presented by Nolan and McGauley (2012). They showed that strong vertical shear introduces much additional complexity to the intensification problem, raising the question as to whether the new intensification paradigm is applicable in the presence of vertical shear. Some guidelines for analyzing the effects of vertical shear were set out in a recent review of what is known about tropical cyclone intensification in the presence of vertical wind shear by Smith and Montgomery (2015). In their review, they suggested that the new intensification paradigm should still provide a useful building block for understanding vortex spin-up in the presence of shear, although one would expect that important modifications to the paradigm would emerge and that eddy flux processes may be especially important.

As a step towards investigating the applicability of the new intensification paradigm in vertical shear, here we analyze a five-day simulation of Hurricane *Earl* using the state-of-the-art
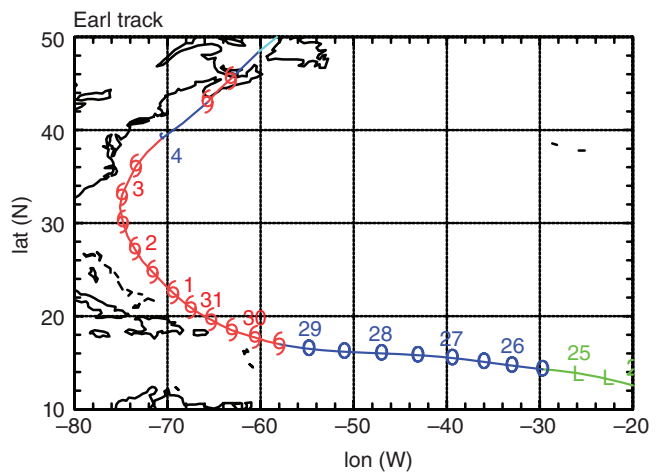

Figure 1. Track of Hurricane *Earl*, 25 August–4 September 2010, based on 'best-track' data from the National Hurricane Center archive. Points marked L over a green track refer to the tropical depression stage, points O over a blue track to the tropical storm stage and the cyclone symbols over a red track denote the hurricane stage. These points are shown at 0000 and 1200 UTC. The numbers adjacent to the letters refer to the day.

Hurricane Weather Research and Forecasting (HWRF)* model. The advantage of using a numerical model simulation to study the dynamics of *Earl* is that it captures the whole period of evolution of the different fields, while observations are limited to certain periods and spatial coverage. The simulation offers the opportunity to appraise further the paradigm in vertical shear including the combined eddy processes (the intrinsic and shear-induced eddy processes) that contribute to the intensification process. We begin by showing that this simulation compares reasonably well with the observations and go on to show that the paradigm is upheld, albeit with appropriate modification.

The remainder of the article is organized as follows. In section 2, we show the best track of Hurricane *Earl* together with the vertical wind shear in its environment during the period of interest. In section 3, we summarize the HWRF model configuration. Aspects of the verification of the *Earl* forecast in terms of traditional metrics as well as metrics of vortex structure are presented in section 4. Section 5 shows the evolution of low-level vorticity during the early part of RI and section 6 examines the thermodynamic support for the intensification process. The dynamics of intensification are investigated in section 7. Conclusions are given in section 8.

2. Hurricane *Earl*

A detailed summary of Hurricane *Earl* and the data collected was provided by Montgomery *et al.* (2014) and only a brief summary is needed here. Hurricane *Earl* originated from a strong tropical wave that left the west coast of Africa on 23 August. The 'best-track' positions of the storm are shown in Figure 1. The observations were carried out during the period 28 August–2 September, as the storm was moving northwestwards prior to recurvature.

Figure 2 shows the evolution of the environmental shear during the period 0000 UTC on 27 August to 0000 UTC on 31 August. The shear is calculated as the difference between the areal average of the wind vectors at 200 and 850 mb over a region within 500 km of the vortex centre (as defined in section 7.1) at 850 mb (DeMaria *et al.*, 2005). The areal average is based on the National Weather Service/National Center for Environmental Prediction (NWS/NCEP) Global Forecasting System (GFS) analysis data. The figure shows that the environmental shear on 28 August is northeasterly, with a magnitude that is relatively large
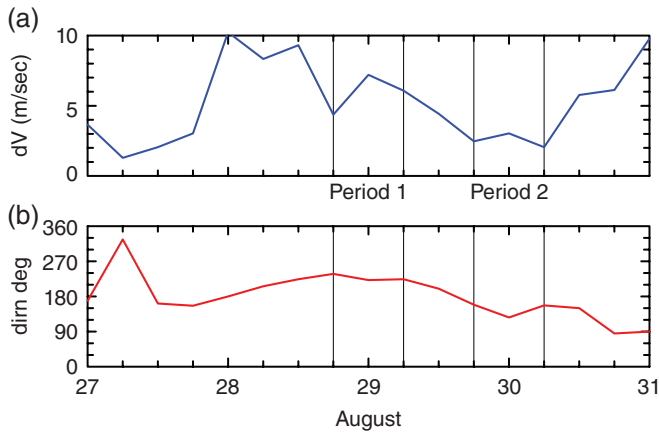
---

*See e.g. Gall *et al.*(2013).

Figure 2. Evolution of the environmental shear during the period 0000 UTC on 27 August to 0000 UTC on 31 August. Panel (a) shows the magnitude of the shear vector and (b) its direction, measured clockwise from north.

($\approx$10 m s^{-1}), but broadly decreases to less than 5 m s^{-1} over the subsequent 2 days as the vortex intensifies rapidly. The increase in shear magnitude after 30 August is presumably a reflection of the development of the outflow anticyclone within the 500 km averaging radius. Despite the relatively large shear, the storm intensified rapidly between 1200 UTC on 28 August and 1200 UTC on 30 August (Figure 3). One objective of this paper is to understand how this RI came about.

3. HWRF simulation of *Earl*

Hurricane *Earl* (2010) was simulated using the triply nested, cloud-resolving version of the operational HWRF system, developed jointly by the National Oceanographic and Atmospheric Administration's NWS/NCEP and the Hurricane Research Division (HRD) of the Atlantic Oceanographic and Meteorological Laboratory as part of the Hurricane Forecast Improvement Project (Gopalakrishnan *et al.*, 2011, 2013; Tallapragada *et al.*, 2014). The version of HWRF used here includes important physics upgrades, including observation-based modifications to the GFS planetary boundary-layer scheme based on observational findings (Zhang *et al.*, 2012, 2015; Gopalakrishnan *et al.*, 2013), improved Geophysical Fluid Dynamics Laboratory surface physics, improved Ferrier microphysics (Ferrier, 1994) and implementation of the new GFS parameterization scheme for shallow convection (Hong and Pan, 1996).

The oceanic component of HWRF is a version of the Princeton Ocean Model adapted for tropical cyclones developed at the University of Rhode Island (Yablonsky and Ginis, 2008). The *Earl* forecast presented in this study is initialized at 1800 UTC on 26 August 2010. This forecast was selected from retrospective forecasts of multiple storms using the 2012 version of the model as part of the Hurricane Forecast and Improvement Project (HFIP)'s high-resolution test conducted at HRD (Zhang *et al.*, 2012). The model physics, boundary and initial conditions are the same as the version used by Chen and Gopalakrishnan (2015), except that all the retrospective forecasts were run with hourly outputs in a cycling mode. Note that Chen and Gopalakrishnan (2015) investigated the asymmetric RI of *Earl* in a sheared environment, with focus on warm-core evolution and convective bursts. Their forecast verification showed that this forecast captured *Earl*'s evolution of intensity, wind-field asymmetry and vortex tilt in terms of both magnitude and direction in comparison with observations.

4. Verification of the *Earl* forecast

Various metrics can be used to assess the integrity of the HWRF forecast for *Earl* described above. First we examine the track and intensity forecasts. The forecast track is shown in Figure 3, where
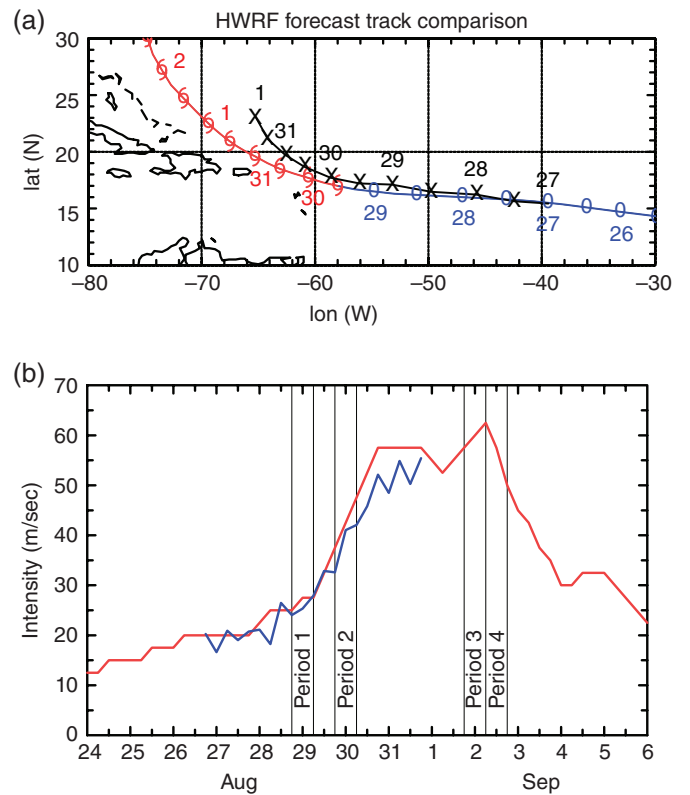

Figure 3. (a) HWRF track forecast for Hurricane *Earl* (2010) in comparison with the best track from the National Hurricane Center. The lettering and colour convention for the best track is the same as in Figure 1. The forecast track is in black and the 12 h storm positions are marked with a cross, with the day above each second cross. (b) Intensity (in terms of maximum near-surface wind speed) forecast in comparison with the best track. Period 2, running from 1800 UTC on 29 August to 0600 UTC on 30 August, is when a relatively large number of dropsonde data are available for analysis.

it is compared with the best track shown in Figure 1. The track is close to that observed for the first four days of the forecast, but the model storm is a little slower than the best track and it begins to recurve a little prematurely. The differences between the best track and forecast positions at 24, 48 and 72 h are 104, 177 and 72 km, respectively, which are within the mean range of track errors at these lead times (see Chen and Gopalakrishnan, 2015). The predicted intensity of *Earl*, characterized by the maximum near surface wind speed (V_{max}) and minimum central pressure are compared with the corresponding quantities derived from the National Hurricane Center's best track in Figure 3(b). Overall the agreement is exceedingly good, the mean error during the forecast period being $\pm$2.4 m s^{-1}, giving some confidence in the integrity of the forecast.

The comprehensive observational data sets obtained in *Earl* enable one to use other metrics besides those described above to assess the forecast. Examples are shown in Figures 4 and 5. Figure 4 compares composite radius–height cross-sections of the azimuthally averaged radial $\langle u \rangle$ and tangential $\langle v \rangle$ wind components and the virtual potential temperature $\langle \theta_v \rangle$ derived from a large number of dropsonde data collected between 1800 UTC on 29 August and 0600 UTC on 30 August with the corresponding azimuthally averaged model output averaged over the same time period. For convenience, the velocity components are calculated in the earth-relative reference frame. The choice of centre for constructing the azimuthal average is discussed in section 7.1. In these cross-sections, the radius is normalized by the radius of maximum tangential wind speed at 2 km altitude, which in the model stays nearly steady with a mean of 32 km and standard deviation of 3.5 km during the 12 h period of averaging. The observational composites are the same as those presented by Rogers *et al.* (2015).

Comparing the left panels of Figure 4 with the corresponding right panels shows that, while the agreement is not perfect, the
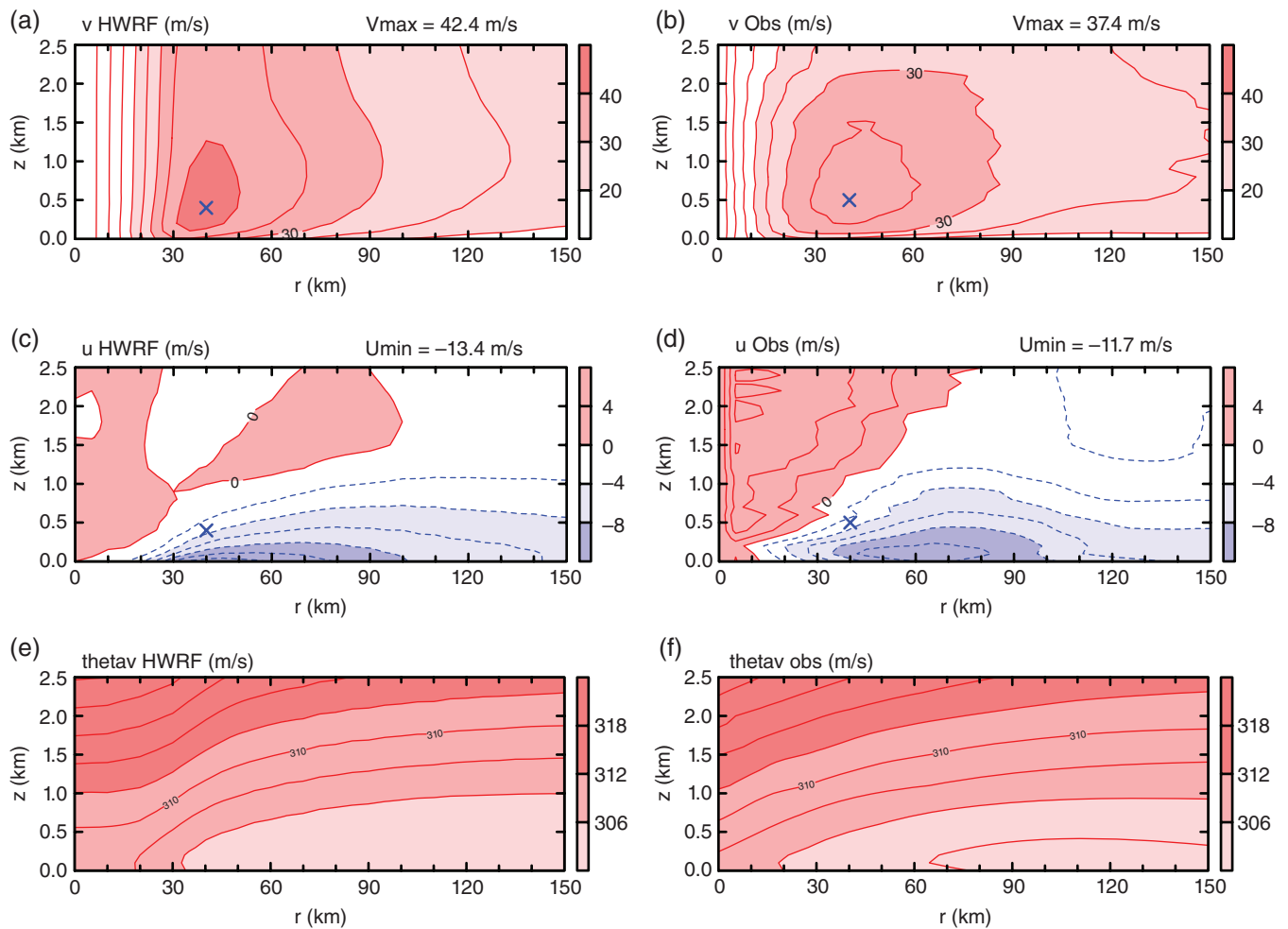
Figure 4. Radius–height plots of (a,b) azimuthally averaged tangential wind $\langle v \rangle$; (c,d) radial wind $\langle u \rangle$; and (e,f) virtual potential temperature $\langle \theta_v \rangle$. The left panels (a), (c), (e) are from the HWRF forecasts, while the right panels (b), (d), (f) are from dropsonde composites. The forecast and observational data are within the same period from 1800 UTC on 29 August to 0600 UTC on 30 August. Contour intervals are 5 m s^{-1} for $\langle v \rangle$, 2 m s^{-1} for $\langle u \rangle$ and 2 K for $\langle \theta_v \rangle$. In (c), the 1 m s^{-1} contour is plotted for $\langle u \rangle > 0$. The location of maximum $\langle v \rangle$ is shown by a blue cross in (a)–(d). Colour shading is as indicated in the side bar.
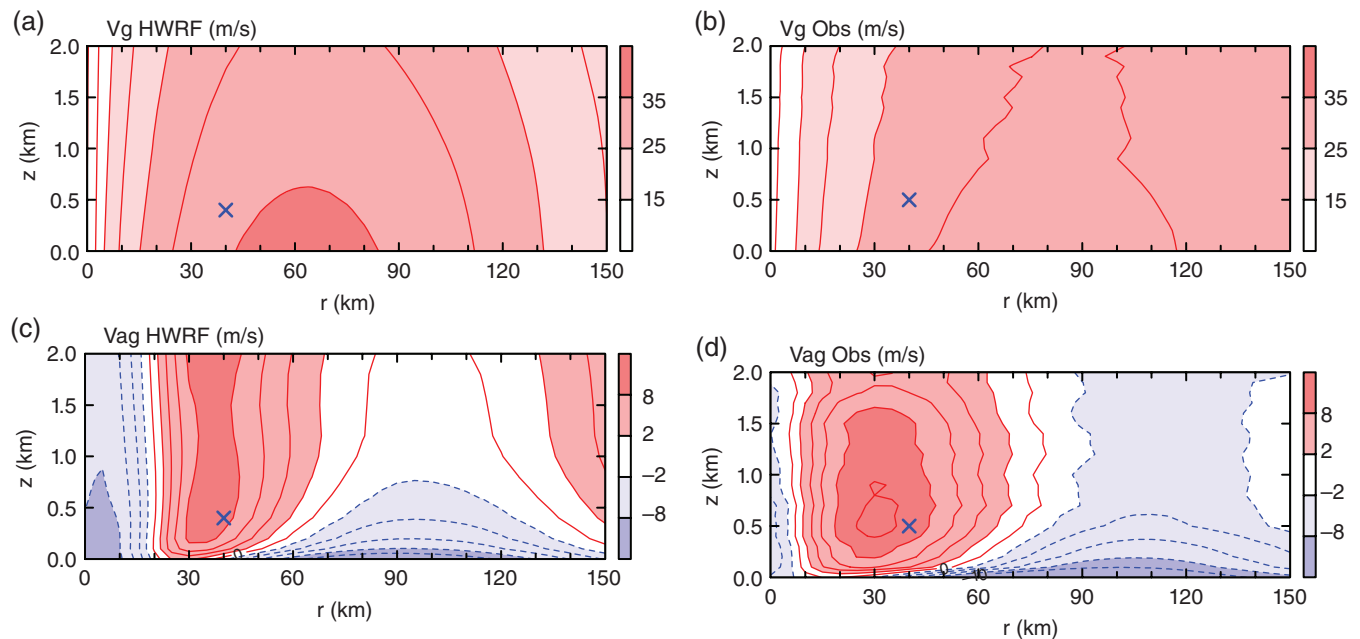

Figure 5. Radius–height plots of (a,b) azimuthally averaged gradient wind ($\langle v_g \rangle$) and (c,d) agradient wind ($\langle v_{ag} \rangle$). The left panels (a), (c) are from the HWRF forecasts, while the right panels (b), (d) are from dropsonde composites. The forecast and observational data are within the same period from 1800 UTC on 29 August to 0600 UTC on 30 August. Contour intervals are 5 m s^{-1} for $\langle v_g \rangle$, 2 m s^{-1} for $\langle v_{ag} \rangle$. Colour shading is as indicated in the side bar.

model does a reasonably good job of capturing the observed structures of $\langle v \rangle$, $\langle u \rangle$ and $\langle \theta_v \rangle$, which themselves will have errors. The maximum value of $\langle v \rangle$ in the model is about 13% stronger than that derived from the observations and the minimum value of $\langle u \rangle$ is such that the maximum inflow is also stronger by about 14%. The maximum outflow is somewhat stronger in the observations, but this is likely to be a reflection of the relatively coarse distribution of wind observations near the storm centre, together with the fact that, in reality, in a vertically sheared storm the flow is not axisymmetric about a vertical axis. Under such conditions, an azimuthal average analysis may not be appropriate near the axis itself.

In both the model and observations, the location of maximum $\langle v \rangle$ (marked by a star in (a)–(d)) is within the inflow layer, a feature that is consistent with the boundary-layer spin-up mechanism discussed in the Introduction. This feature is consistent also with the composite analysis of hundreds of dropsondes from multiple hurricanes (Zhang *et al.*, 2011a). The similarity in the $\langle \theta_v \rangle$ structures is encouraging, because previous studies using an earlier version (pre-2012) of the HWRF model had a much warmer and more moist structure in the boundary layer (Zhang *et al.*, 2012). After adjusting the vertical diffusion in the boundary-layer scheme of HWRF using observations from Zhang *et al.* (2011b), the simulated thermal structure shown here is much improved.

As noted earlier, the focus of this article is on the spin-up of Hurricane *Earl* during its RI phase. Figure 5 compares the simulated azimuthally averaged gradient and agradient wind components. The latter are defined as the departure of gradient wind from $\langle v \rangle$, with the corresponding fields derived from the observations during the same 12 h period as in Figure 4. The gradient wind is calculated by solving the quadratic equation expressing axisymmetric gradient wind balance in terms of the radial pressure gradient force per unit mass (see Montgomery *et al.* (2014) and Rogers *et al.* (2015) for details). It is seen that the model captures the regions of observed supergradient winds in and near the eyewall and subgradient winds outside the eyewall. The agreement between the model and observational composites is quantitatively good. The difference is mainly in the magnitude of the agradient wind, where the modelled value is a little smaller than observed. This difference may be due to the fact that the data coverage of the observations is not as large as in the model, so more smoothing is in the modelled fields. However, given the limitations of both the model and the observational analysis, it is not possible to say which of the fields is closest to reality. Even so, this result, in combination with the comparisons in Figure 4, suggests that the model simulation is adequate to study the spin-up processes of Hurricane *Earl*.

5. Synopsis of vorticity organization

Figure 6 shows the evolution of the relative vorticity at a height of 1.5 km during the early period of RI (57–62 h) with the wind vectors and contours of vertical velocity with a magnitude of $0.5 \, \text{m s}^{-1}$ superimposed. These vertical velocity contours show the location of the roots of the updraughts. It is evident that vortical convective cells, highly asymmetric in nature, are ubiquitous throughout the period shown. In the inner core region of the vortex, the roots of the updraughts are largely associated with the cyclonic vorticity maxima and related vorticity filamentary structures, indicating that these vorticity features are the result of vortex tube stretching as individual convective cells intensify. However, the convectively intensified vorticity lingers after each cell has collapsed. Animations of these fields show that the lingering vorticity anomalies move inwards. This inward movement is presumably caused in part by the diabatically driven system-scale secondary circulation above the frictional boundary layer and in part by upgradient vorticity transport associated with vortex Rossby-wave-like axisymmetrizing disturbances inside the radius of maximum tangential wind speed.

While the vortex axisymmetrization process does not change the net absolute circulation within a fixed circuit around the convective region, the shearing of convectively generated cyclonic vorticity anomalies around the parent circulation contributes to consolidating the convectively generated cyclonic vorticity anomalies into a single monopole of cyclonic vorticity (Melander *et al.*, 1987; Montgomery and Enagonio, 1998; Chen and Yau, 2001; Enagonio and Montgomery, 2001; Chen *et al.*, 2003; McWilliams *et al.*, 2003). These processes will be discussed and quantified in part in section 7.4.

Farther outside of the core region, the updraughts are often straddled by small-scale cyclonic/anticyclonic vorticity anomalies. These dipole-like small-scale vorticity structures are presumably the result of vortex-tube tilting processes that would tend to dominate the vortex-tube stretching process in regions of relatively low cyclonic vorticity (e.g. Kilroy and Smith, 2016).

6. Thermodynamic support

The new paradigm for tropical cyclone spin-up requires a modest elevation of low-level moisture to sustain deep convection in the inner core region but, as shown in Montgomery *et al.* (2009), spin-up does not depend essentially on a progressive increase of the surface moisture fluxes with wind speed (the so-called Wind-Induced Surface Heat Exchange (WISHE) feedback mechanism[†]). It has become common practice to use pseudo-equivalent potential temperature[‡] instead of water-vapour mixing ratio to characterize moisture content. This is because θ_e is approximately conserved in the absence of mixing processes, in both dry and moist ascent, and because θ_e increases monotonically with moisture content.

A further requirement for spin-up is the existence of a sufficiently moist pouch several hundred kilometres in horizontal extent, so that deep convection is protected to a large degree from the detrimental effects of the entrainment of relatively dry air (Riemer and Montgomery, 2011). Analyses have verified that *Earl* had such a protected environment in the mid to lower troposphere prior to and during *Earl*'s period of RI (M. Boothe, 2016, personnal communication).

Figure 7 shows horizontal cross-sections of θ_e at the lowest model level in the middle of the two time periods in Figure 2. Two contours of vertical velocity are shown also to highlight the convective updraughts and mesoscale downdraughts. The convective updraughts are identified by the $0.5 \, \text{m s}^{-1}$ contour of vertical velocity at the 5 km level. The mesoscale downdraughts are identified by the $-0.1 \, \text{m s}^{-1}$ contour at the 1.5 km level, the lower level in this case being suitable to reflect the downward transport of low-θ_e air into the boundary layer. The area-averaged vertical shear direction and magnitude taken from Figure 2 are indicated in the upper left portion of each panel. In the middle of Period 1, panel (a) shows a central moist envelope region of elevated θ_e that is partially surrounded by a region of air with depressed θ_e. Relative to the vertical shear vector, the convective updraughts are confined primarily to a downshear-left region of the inner-core vortex. The mesoscale downdraughts are located downwind of these updraughts, but on the upshear side of the vortex. This orientation of updraught, downdraught and θ_e deficit is consistent with that found by Riemer *et al.* (2010, section 4; 2013) in their idealized simulation of an intensifying hurricane subject to the imposition of a unidirectional vertical shear acting on the vortex circulation.

[†]The WISHE mechanism for tropical cyclone intensification is based on the idea of an air−sea interaction instability comprising a postulated multi-step feedback loop involving, in part, the near-surface wind speed and the evaporation of water from the underlying ocean, with the evaporation rate being a function of wind speed and thermodynamic disequilibrium. While the WISHE mechanism is widely held to be the explanation as to how tropical cyclones intensify, it has been shown to be unneccesary to explain the essential physics of tropical cyclone intensification (Montgomery *et al.*, 2009, 2015).
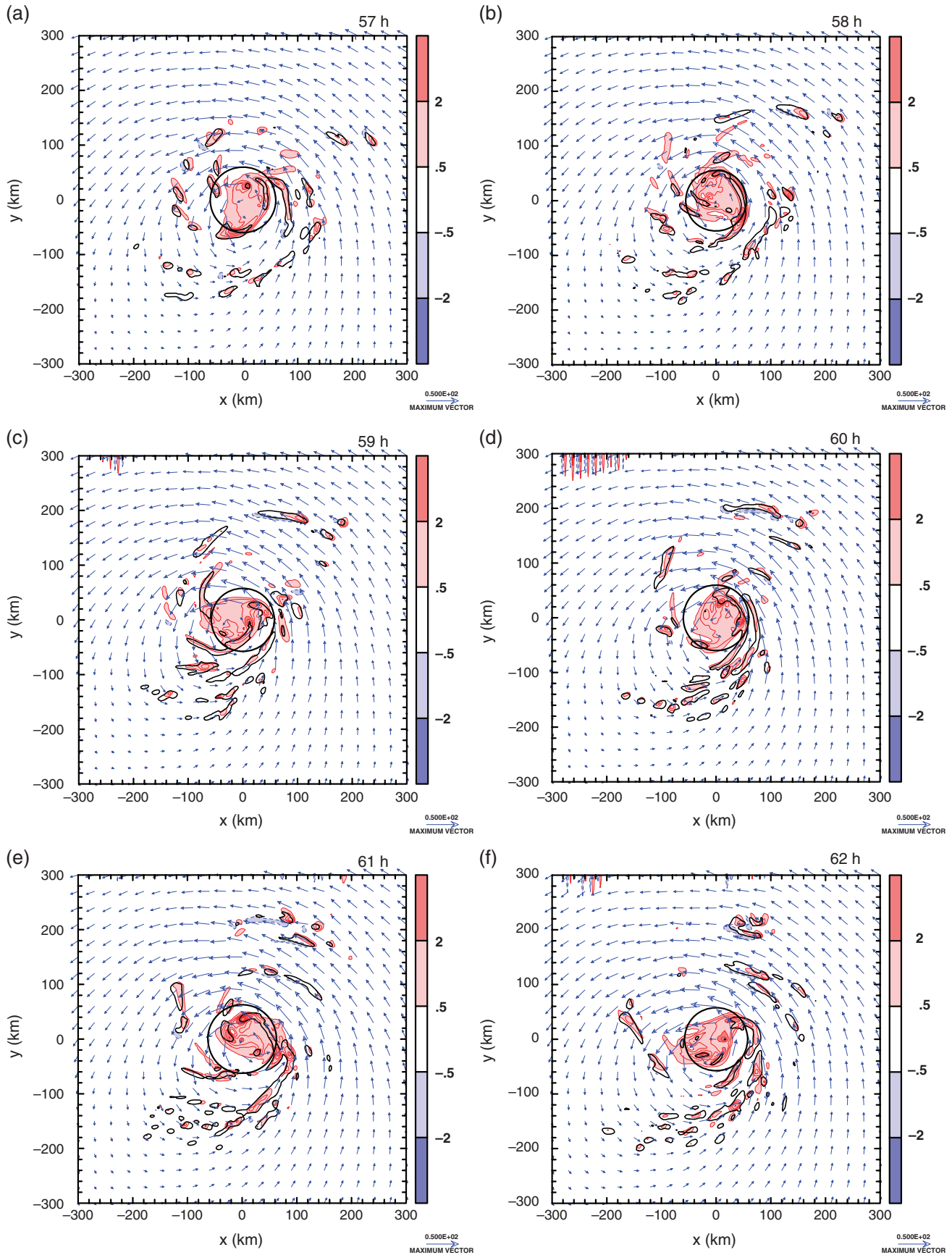[‡]θ_e is calculated using Bolton's formula (Bolton, 1980; eq. 43).

Figure 6. Horizontal plot of the relative vorticity (ζ) at 1.5 km altitude at hourly intervals (a)–(f) from 57–62 h during the early period of RI (57–63 h in the simulation), with the wind vectors and contours of vertical velocity with a magnitude of 0.5 m s^{-1} superimposed. The black circle represents the radius of maximum wind speed. The contour interval for ζ is 5 × 10^{-4} s^{-1}. Colour shading is as indicated in the side bar in multiples of 1 × 10^{-3} s^{-1}.

ⓒ 2016 The Authors. *Quarterly Journal of the Royal Meteorological Society*
published by John Wiley & Sons Ltd on behalf of the Royal Meteorological Society.

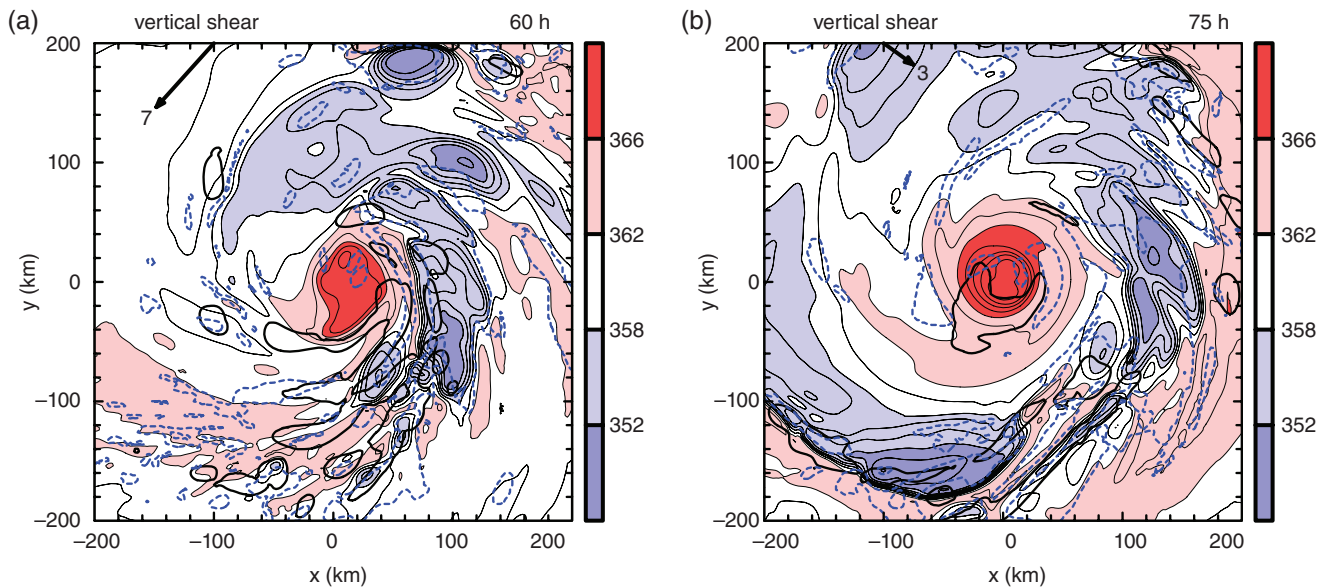*Q. J. R. Meteorol. Soc.* **143**: 293–308 (2017)

Figure 7. Horizontal cross-sections of θ_e at the lowest model level at (a) 60 h and (b) 75 h. Contour interval 2 K. Colour shading levels are indicated on the side bar. Thick black curves are the $0.5\,\mathrm{m\,s^{-1}}$ contours of vertical velocity at a height of 5 km and thick blue dashed curves are the $-0.1\,\mathrm{m\,s^{-1}}$ contours of vertical velocity at a height of 1.5 km.

Figure 7(b) shows the same variables in the middle of Period 2. At this time, the vortex is intensifying rapidly and the area-averaged vertical shear has decreased by more than half its value during Period 1. Note that, while the area of relatively low θ_e surrounding the storm has increased, so has the area and magnitude of elevated θ_e in the inner core region. This increase is necessary to support the thermodynamics of intensification, as discussed below.

To demonstrate that there is increasing thermodynamic support for the intensification of Hurricane *Earl*, we show in Figure 8 a Hovmöller diagram of the azimuthally averaged θ_e of air at the lowest model level (approximately 30 m). The figure shows also the location of the radius of maximum tangential wind speed (RMW) based on an average of the azimuthally averaged tangential wind field between 1 and 2 km height. During the two periods of intensification analyzed, there is a marked negative radial gradient of θ_e inside the RMW. In contrast, beyond the RMW the negative radial gradient of θ_e is much weaker, presumably on account of convective and mesoscale downdraughts, which bring relatively dry air into the boundary layer from above to counter the moisture evaporated from the surface (Carrier *et al.*, 1971; Rotunno and Emanuel, 1987; Riemer *et al.*, 2010). Perhaps the most prominent feature is the progressive elevation in θ_e inside the RMW to the end of the calculation, commencing a little before the first intensification period analyzed.

In the new intensification paradigm, an increase in near-surface θ_e is required to maintain the buoyancy of deep convection in the region where air is being lofted from the boundary layer into the eyewall. The maintenance of buoyant deep convection is a prerequisite[§] for convection to ventilate the increasing amount of air being lofted from the boundary layer as the vortex intensifies and the upper-level warm core aloft strengthens (Kilroy *et al.*, 2015).

The foregoing ideas relating to thermodynamic processes differ from the more limiting view in the classical theory of intensification based on axisymmetric balance dynamics. In this theory, the intensification is a result of inward moving M-surfaces above the boundary layer, where M is materially conserved. This inward movement is a consequence of the collective action of deep convection, which in the model is represented by a spatial distribution of the diabatic heating rate, $\dot{\theta}(r, z)$. The secondary circulation that moves the M-surfaces is forced primarily by the radial gradient of diabatic heating, $\partial \dot{\theta}/\partial r$. Since $\partial \dot{\theta}/\partial r$ depends not only on the radial gradient of θ_e, but also on the radial distribution of vertical velocity,[¶] w, no explicit functional relation between $\partial \dot{\theta}/\partial r$ and $\partial \theta_e/\partial r$ exists. In other words, $\partial \theta_e/\partial r$ does not determine $\partial \dot{\theta}/\partial r$ a priori without prior knowledge of the vertical velocity.[‖] Clearly, one cannot infer that the elevation of inner-core θ_e shown in Figure 8 equates to a sufficiently negative radial gradient of $\dot{\theta}$ over a sufficient depth to force a secondary circulation capable of producing vortex spin-up. However, for the reasons given in the preceding paragraph, some elevation of low-level θ_e is necessary to support continued deep convection in an intensifying vortex. These issues are worth bearing in mind when interpreting the model-derived structures of θ_e in relationship to the classical theory of intensification.

7. Dynamics of intensification

We examine now the dynamical processes involved in the intensification process. First we provide an azimuthally averaged view of spin-up and go on to examine the role of eddies. To do this, we follow closely the methodology presented in Persing *et al.* (2013). Namely, we diagnose both the mean and eddy contributions to the tendency of tangential and radial velocity (see their section 6). Our basic approach is to employ a vortex-centric description of the vortex evolution using a cylindrical polar coordinate system. Such a description is advantageous because of the approximate circular symmetry of the basic vortex in the bulk of the troposphere.

7.1. Choice of vortex centre

A cylindrical coordinate system requires the choice of an origin of coordinates. Although the equations are valid for any centre

---

[§]The ability of deep convection to ventilate the mass that is expelled by the boundary layer depends on the convective mass flux and the mass flux must depend *inter alia* on the buoyancy of the cloud updraughts. However, it also depends on the area of the updraughts. Clearly one needs to calculate the changes in convective mass flux using a numerical model (see e.g. Kilroy *et al.*, 2015).

[¶]The diabatic heating rate, $\dot{\theta} = D\theta/Dt$, is approximately related to the vertical velocity w and equivalent potential temperature θ_e by the formula $\dot{\theta} = \mu w$, where $\mu = -L(\partial q_v/\partial z)_{\theta_e=constant}$, where L is the latent heat of condensation and q_v is the water-vapour mixing ratio.

[‖]An alternative approach is to formulate the balanced evolution in terms of moist equivalent potential temperature instead of dry potential temperature. A particularly elegant method within this framework is to assume that air parcels rising out of the boundary layer materially conserve their equivalent potential temperature.
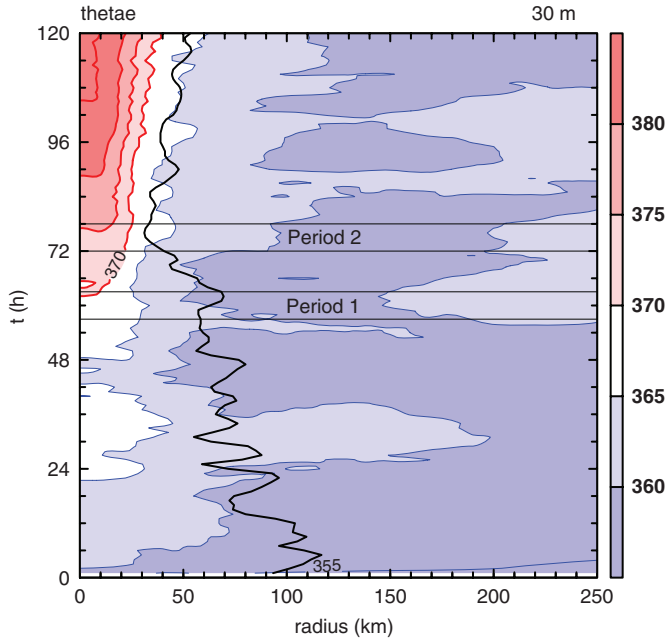
Figure 8. Radius–time diagram showing contours of azimuthally averaged θ_e at the lowest model level (approximately 30 m). Contour interval 5 K. Also shown is the location of the RMW, based here on an average of the azimuthally averaged tangential wind field between 1 and 2 km in height. The two periods of intensification discussed in the text, Periods 1 and 2, are indicated by thin horizontal lines.

of coordinates, even if the vortex is tilted, the analysis is likely to be best for a weakly tilted vortex. However, just as in the case of a barotropic vortex, the structure of the axisymmetric vortex and its asymmetries depends on the arbitrary choice of a centre (Smith *et al.*, 1990). In practice, one wishes to reduce complexity by choosing a centre that effectively minimizes the asymmetric representation of the vortex flow. As in the barotropic case, there is no unique way to do this in general and a choice has to be made to achieve a solution that minimizes some metric of asymmetry. Even for an initially axially symmetric circulation, a simple tilt of the vortex flow will produce intrinsic asymmetries that cannot be entirely eliminated. Here we choose to define the centre as the location of minimum surface pressure and we use the same centre at all heights. The results shown herein are found to be robust to small changes in the chosen centre and are therefore considered physically meaningful.

7.2. Mean and eddy partitioning of the horizontal momentum equations

In the analysis that follows, we apply the traditional Eulerian approach to 'eddy-mean' partitioning as discussed in Persing *et al.* (2013), but apply this to both horizontal momentum equations. In cylindrical polar coordinates, the tangential momentum equation has the form

$$\frac{\partial v}{\partial t} = -u\frac{\partial v}{\partial r} - \frac{v}{r}\frac{\partial v}{\partial \lambda} - w\frac{\partial v}{\partial z} - \left(f + \frac{v}{r}\right)u$$
$$-\frac{1}{\rho r}\frac{\partial p}{\partial \lambda} + D_v, \qquad (1)$$

where (u, v, w) are the velocity components in the cylindrical coordinate system (r, λ, z), t denotes time, ρ is the density, p is the pressure, f is the Coriolis parameter (assumed here to be constant for simplicity) and D_v is the subgrid-scale forcing of v (including diffusive tendencies in the interior flow and the boundary layer).

The corresponding radial momentum equation is

$$\frac{\partial u}{\partial t} = -u\frac{\partial u}{\partial r} - \frac{v}{r}\frac{\partial u}{\partial \lambda} - w\frac{\partial u}{\partial z} + \left(fv + \frac{v^2}{r}\right)$$
$$-\frac{1}{\rho}\frac{\partial p}{\partial r} + D_u. \qquad (2)$$

The azimuthal mean of some quantity Q is defined by

$$\langle Q(r, z, t)\rangle = \frac{1}{2\pi}\int_0^{2\pi} Q(r, \lambda, z, t)\, d\lambda, \qquad (3)$$

where λ is the azimuth (in radians). Applying this operator to Eqs (1) and (2) gives the equations for the azimuthally averaged tangential and radial wind tendencies:

$$\frac{\partial \langle v\rangle}{\partial t} = \underbrace{-\langle u\rangle\langle f + \zeta\rangle}_{V_{m\zeta}} \quad \underbrace{-\langle w\rangle\frac{\partial \langle v\rangle}{\partial z}}_{V_{mv}} \quad \underbrace{-\langle u'\zeta'\rangle}_{V_{e\zeta}} \qquad (4)$$
$$\underbrace{-\left\langle w'\frac{\partial v'}{\partial z}\right\rangle}_{V_{ev}} + \underbrace{\left\langle -\frac{1}{\rho r}\frac{\partial p'}{\partial \lambda}\right\rangle}_{V_{ppg}} + \underbrace{\langle D_{dh}\rangle}_{V_{dh}} + \underbrace{\langle D_{dv}\rangle}_{V_{dv}},$$

$$\frac{\partial \langle u\rangle}{\partial t} = \underbrace{-\langle u\rangle\frac{\partial \langle u\rangle}{\partial r}}_{U_{mr}} \quad \underbrace{-\langle w\rangle\frac{\partial \langle u\rangle}{\partial z}}_{U_{mv}}$$
$$\underbrace{+f\langle v\rangle + \frac{\langle v\rangle^2}{r} - \frac{1}{\langle\rho\rangle}\frac{\partial \langle p\rangle}{\partial r}}_{U_{magf}}$$
$$\underbrace{-\left\langle u'\frac{\partial u'}{\partial r} + \frac{v'}{r}\frac{\partial u'}{\partial \lambda}\right\rangle}_{U_{eh}} \quad \underbrace{-\left\langle w'\frac{\partial u'}{\partial z}\right\rangle}_{U_{ev}}$$
$$\underbrace{+\left\langle -\frac{1}{\rho}\frac{\partial p'}{\partial r} + \frac{v'^2}{r}\right\rangle}_{U_{eagf}} + \underbrace{\langle D_u\rangle}_{U_d}, \qquad (5)$$

where the prime denotes a departure from the azimuthal mean (or 'eddy') and ζ is vertical component of relative vorticity. The highlighted terms on the right-hand side of Eq. (5) are as follows:

- $V_{m\zeta}$ is the mean radial influx of absolute vertical vorticity;
- V_{mv} is the mean vertical advection of mean tangential momentum;
- $V_{e\zeta}$ is the mean radial eddy vorticity flux;
- V_{ev} the mean vertical advection of eddy tangential momentum;
- V_{ppg} is the mean azimuthal perturbation pressure gradient force per unit mass; and
- V_{dh} and V_{dv} are the mean horizontal and vertical diffusive tendencies, respectively.

On the right-hand side of Eq. (5), the terms are as follows:

- U_{mr} is the mean radial advection of mean radial momentum;
- U_{mv} is the mean vertical advection of mean radial momentum;
- U_{magf} is the mean agradient force per unit mass;
- U_{eh} is the mean eddy horizontal advection of radial momentum;
- U_{ev} is the mean eddy vertical advection of radial momentum;
- U_{eagf} is the mean eddy agradient force per unit mass; and

- U_d is the combined mean horizontal and vertical diffusive tendency.

It is worth pointing out that, in the foregoing partitioning method, highly localized asymmetric features will project to a degree on to what are defined here as 'mean' terms. For example, if a single, large-amplitude, positive anomaly in vertical motion is imposed on an otherwise axisymmetric vortex, the anomaly will project on to both the vertical eddy and mean terms. An example is shown in Kilroy and Smith (2016).

7.3.   The effects of mean processes

As discussed in the Introduction, spin-up in the classical model for tropical cyclone intensification is associated with the convergence of the M-surfaces above the boundary layer, where, to a first approximation, M is materially conserved. Note that, in terms of M, $\langle v \rangle = M/r - \frac{1}{2}fr$. Moreover, the convergence of the M-surfaces is a result of the secondary overturning circulation induced by deep convection in the inner core region of the storm. It is of interest, therefore, to examine the evolution of the M-surfaces in the HWRF simulation.

Because the change in the latitude of the moving storm is small ($<0.6°$) during the period of interest (see Figure 1), the change in f associated with the storm movement is small ($<3\%$). For this reason, we treat f as a constant, equal to the value at the mean latitude during this period.

Figure 9 shows the radius–height structure and evolution of the azimuthally averaged M-surfaces spanning Periods 1 and 2 of *Earl*'s RI phase. The left panels show the M fields from the HWRF model and the right panels show the corresponding fields derived from aircraft Doppler radar (Montgomery *et al.*, 2014; Rogers *et al.*, 2015). (The aircraft analyses were presented in Montgomery *et al.* (2014), but are repeated here for comparison with the HWRF simulation in the right panels of Figure 9.)

Prominent structural features are that M increases with radius at each level at each time, implying that the vortex is centrifugally (or inertially) stable (e.g. Franklin *et al.*, 1993; Shapiro and Montgomery, 1993) and that the M-surfaces slope inwards with decreasing radius within the boundary layer and outwards with radius aloft. These slopes give rise to a nose-like feature near the top of the boundary layer. This structure of the M-surfaces may be understood as follows. Above the boundary layer, the azimuthally averaged tangential wind component is close to gradient wind balance and thermal wind balance. Thus, because the tropical cyclone vortex is warm-cored, the M-surfaces lean outwards there. The inward slope of the M-surfaces at low levels is a manifestation of the reduction of $\langle v \rangle$ and hence M by the frictional torque at the surface and the corresponding turbulent diffusion of $\langle v \rangle$ to the surface.

The shading in Figure 9 is used to highlight the movement of the M-surfaces. It is seen that, in both the model and the observations, the M-surfaces move radially inwards below a height of 12 km and, because $\langle v \rangle = M/r - \frac{1}{2}fr$, the tangential winds are amplified at these levels.

We examine now some aspects of the boundary layer that are not part of the classical spin-up model. In the outer region of the vortex, where the radial advection of momentum in the boundary layer is not dominant, the tangential wind is reduced locally by friction. Then, because the radial pressure gradient in the boundary layer is essentially independent of height, there is an inward-directed agradient force, defined as the departure from the balance between the pressure gradient, Coriolis force and centrifugal force. As the radius decreases, the radial advection of tangential momentum in the boundary layer becomes progressively more important and, as explained in the Introduction, if air parcels converging in this layer can reach small radii without losing too much M, it is possible that larger tangential winds can be achieved in the boundary layer than in the free atmosphere above. When this happens, the winds are supergradient because

those above the boundary are nominally in gradient wind balance, except possibly at radii where these supergradient winds are lofted into the eyewall. The features were confirmed by observations in Hurricane *Earl* by Montgomery *et al.* (2014).

The foregoing ideas are underpinned by the radius–time plot of the azimuthally averaged agradient force (U_{magf} in Eq. (5)) at a height of 500 m shown in Figure 10. Also shown in this figure are the location of the RMW, based on an average of the azimuthally averaged tangential wind field between 1 and 2 km in height, and the two periods of RI, as in Figure 7. Before the first of the RI periods, there is an extensive region outside the RMW in which U_{magf} is weakly negative and there are a few patches inside this radius where U_{magf} is positive. As the vortex strengthens, the region of negative U_{magf} extends outwards with time and strengthens in a widening band just outside the RMW. Concurrently, the positive values also strengthen and become more coherent inside the RMW. In summary, the agradient force changes sign at some radius near the RMW. The radial patterns of the agradient force in Figure 10 corroborate the low-level structure of the supergradient winds in the radius–height cross-sections in Figure 5(c).

The sharpening of the nose of the M-surfaces with decreasing radius seen in Figure 9 is an indication of the increasingly strong radial advection of the M-surfaces within the boundary layer. In the Montgomery *et al.* (2014) study, we were cautious of attributing much significance to the tendency of the M-surfaces to bow inwards near 2 km altitude outside the RMW on account of the difficulty of extracting Doppler data at low altitudes. However, it is seen here that the HWRF simulations support this feature.

It is fair to point out that the basis for the boundary-layer spin-up mechanism has been challenged by Kepert (2012, see the first paragraph on p1442). Kepert argued that, based on his *steady*** boundary-layer solutions, the bulk boundary-layer scheme used in numerical calculations to underpin the mechanism 'leads to an excessively strong inflow and updraught, thereby exaggerating the inward advection of angular momentum within the inflow layer, the strength of the supergradient flow, and the rate at which it is advected upward'. Notwithstanding the fact that prior numerical model simulations by Smith and Thomsen (2010) using five different boundary-layer schemes confirmed the robustness of the boundary-layer spin-up mechanism, the results presented here provide additional support for this mechanism.

7.4.   Quantification of mean and eddy processes

We turn now to quantify the role of various processes in the new paradigm for intensification in the presence of vertical shear. As discussed in Smith and Montgomery (2015), vertical shear acts to tilt the vortex (Jones, 1995) and excite vortex Rossby waves (Reasor *et al.*, 2004; Reasor and Montgomery, 2015, and references therein), which accounts in part for the evolution of the tilt. These vortex Rossby waves couple with the boundary layer and deep convection and generally induce a myriad of smaller-scale asymmetric motions including localized convective updraughts and downdraughts, etc. (Riemer *et al.*, 2010, 2013 and references therein). Both the waves and the asymmetric motions they generate will project collectively on to the azimuthally averaged view of the new intensification paradigm in the form of eddy terms in the equations of motion. Of course, the vortex Rossby waves themselves cannot be described in terms of azimuthally averaged dynamics, so that the azimuthally averaged view is only part of the intensification problem. For simplicity, we will focus here solely on the projection of these eddy processes on the azimuthally averaged dynamics.

**Smith and Montgomery (2010) showed that solutions of the steady boundary-layer equations are over-constrained in the inner core of the vortex by the need to impose boundary conditions on the horizontal velocity components where the flow exits the boundary layer. Mathematically, this is an open boundary at which the velocities should be determined by the solution itself. For this reason, there is an inconsistency in using a multilevel steady boundary-layer model to critique the integrity of the boundary layer spin-up mechanism.
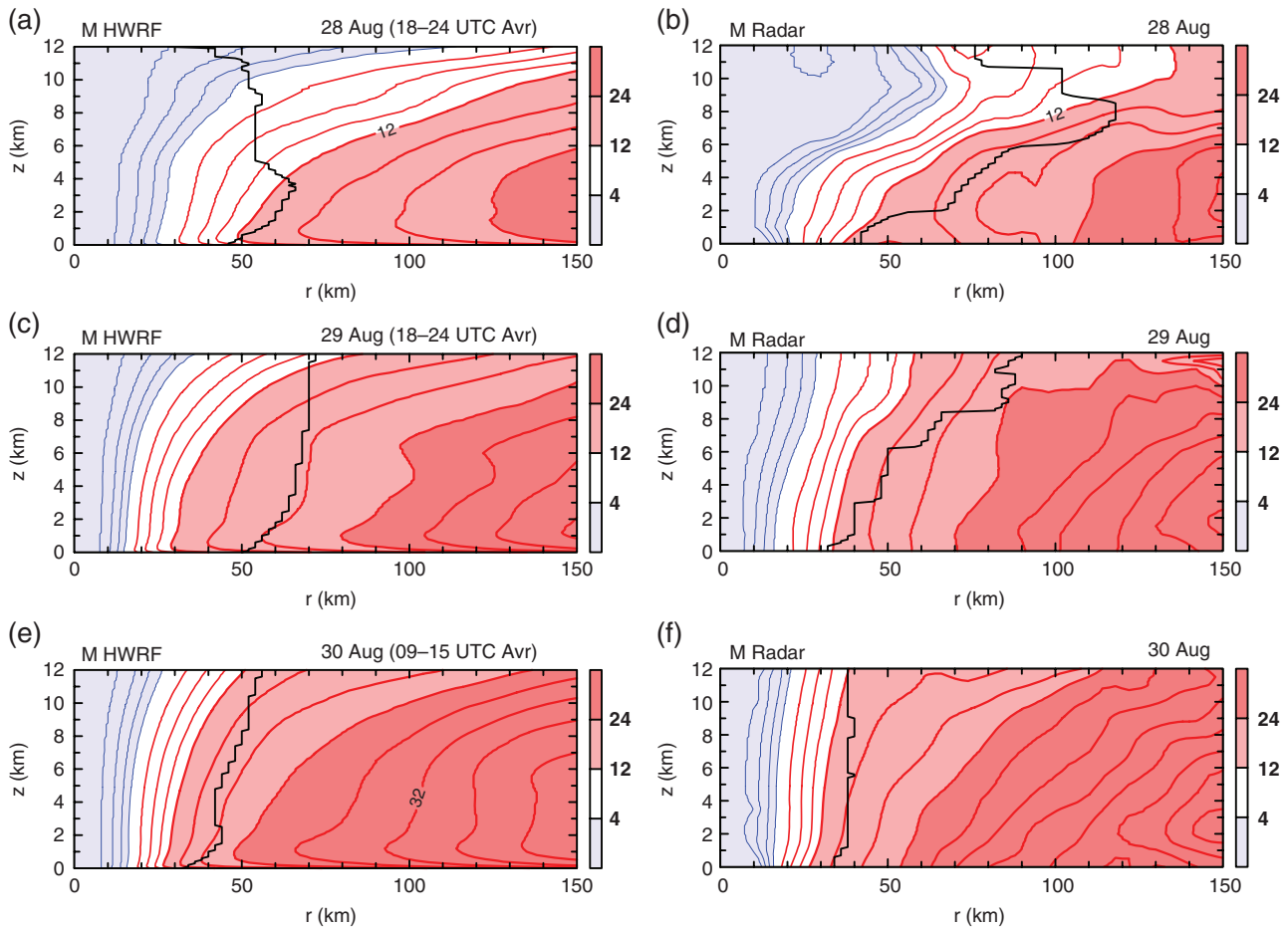
Figure 9. Radius–height plots of (azimuthally averaged) absolute angular momentum, M, over a 6 h period centred at (a) 2200 UTC on 28 August, (c) 2200 UTC on 29 August and (e) 1200 UTC on 30 August (right) from the HWRF forecasts. Panels (b), (d) and (f) are from Doppler radar composites at the corresponding times. Contour interval for $\langle M \rangle$: 1×10^5 m^2 s^{-1}. Colour shading is as indicated in the side bar in multiples of 1×10^5 m^2 s^{-1}. The thick black curves show the radial location of the maximum azimuthally averaged tangential wind speed as a function of height.
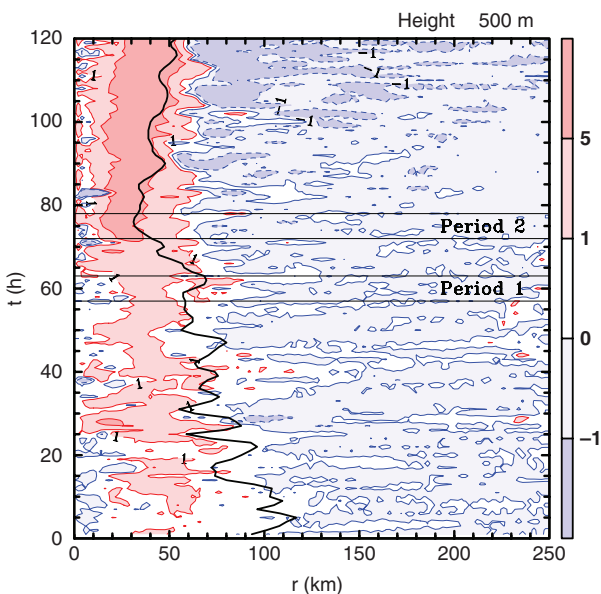
Figure 10. Time–radius plot of the azimuthally averaged agradient force, U_{magf}, at a height of 500 m as a function of forecast time in hours. Contour interval 10^{-3} m s^{-1}. The thick black curve shows the radial location of the maximum azimuthally averaged tangential wind speed averaged over the height range 1–2 km.

7.4.1. Period 1

Figure 11 shows time averages of all but one of the terms in the azimuthally averaged tangential momentum equation (Eq. (3)) during the early period of RI (between 57 and 63 h, i.e. Period 1 of Figure 3). The term not shown is the azimuthal average of

the azimuthal perturbation pressure gradient force per unit mass (term V_{ppg} in Eq. (5)), which is much smaller than the other terms because the azimuthal variation in density is small. For orientation, the figure shows also the corresponding radial and tangential velocity fields and the main updraught region. Further, each panel shows the location of the RMW as a function of height.

The contributions to the tangential wind tendency shown in Figure 11 are the mean vorticity influx (c), the mean vertical advection of tangential velocity (d), their sum (e), the sum of the radial and vertical eddy terms $V_{e\zeta} + V_{ev}$ (f), the contributions to the subgrid-scale tendency from the horizontal V_{dh} and vertical V_{dv} diffusion (g) and (h), the sum of all these tendencies (i) and finally the calculated tangential wind tendency $\partial \langle v \rangle / \partial t$ (j), calculated as the time average of a centred time difference over a 2 h period at each time in the average. In (g) and (h), V_{dh} and V_{dv} are calculated explicitly following the methodology of Persing *et al.* (2013), but using the formulation of these diffusion processes in the HWRF model (Zhang *et al.*, 2015, section 2). It turns out that V_{dh} is relatively small (note that the contour interval in Figure 11(g) is an order of magnitude smaller than in all other panels).

At this stage of development, the tangential wind field has the typical structure of a warm-cored vortex, with wind speed decreasing with height above some shallow friction layer (Figure 11(a)). The radius of maximum tangential wind speed tends to increase with height, albeit with some fluctuation. There is weak radial inflow throughout much of the lower troposphere, with radial outflow above (Figure 11(b)). The strongest inflow is confined to a shallow layer (less than 1 km) near the surface and the largest outflow occurs at an altitude of 14 km. There is a broad region of mean ascent exceeding 0.2 m s^{-1} between about
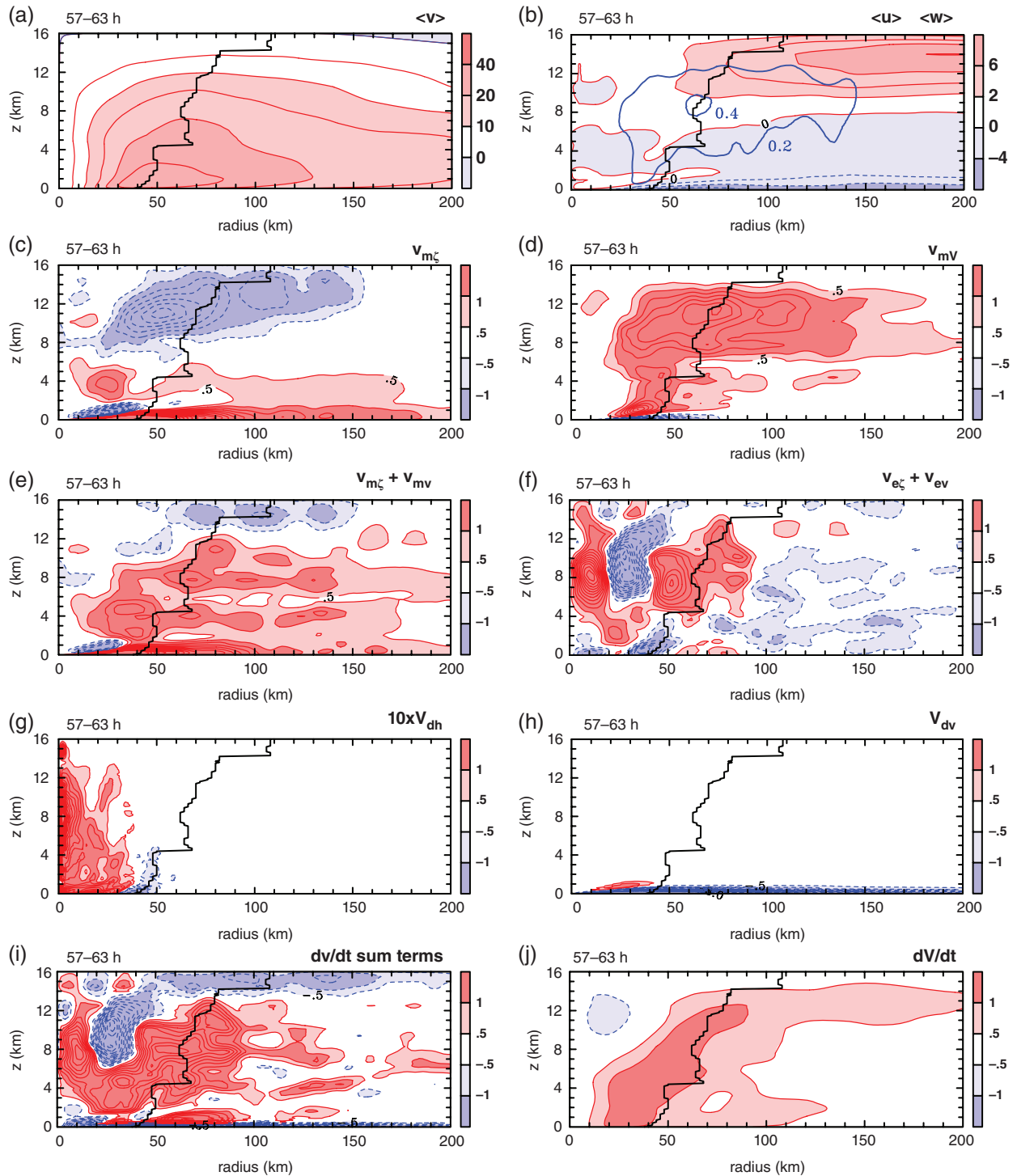
© 2016 The Authors. *Quarterly Journal of the Royal Meteorological Society* published by John Wiley & Sons Ltd on behalf of the Royal Meteorological Society.

Q. J. R. Meteorol. Soc. **143**: 293–308 (2017)

Figure 11. Radius−height plots of azimuthally averaged (a) tangential and (b) radial wind components, together with terms in the azimuthally averaged tangential wind tendency equation during the period 57−63 h: (c) mean absolute vorticity influx $V_{m\zeta}$, (d) mean vertical advection of tangential momentum V_{mv}, (e) the total mean advective tendency $V_{m\zeta} + V_{mv}$, (f) sum of the radial and vertical eddy advection terms $V_{e\zeta} + V_{ev}$, (g) horizontal (subgrid-scale) diffusive tendency V_{dh}, (h) vertical (subgrid-scale) diffusive tendency V_{dv}, (i) the sum of all tendency terms, (j) the tangential wind tendency dV/dt (calculated as the time average of a centred time difference over a 2 h period at each time in the average). Red colours denotes positive values; blue colours (dashed contours) denote negative values. Contour interval: 5 m s^{-1} for tangential wind component, 2 m s^{-1} for radial wind component, 0.5 m s^{-1} h^{-1} for all tendency terms, except in (g), where the interval is 0.05 m s^{-1} h^{-1}. Colour shading is as indicated in the side bar in units of m s^{-1} h^{-1}. The solid blue contours in (b) show regions of positive azimuthally averaged vertical velocity exceeding 0.2 and 0.4 m s^{-1}, as indicated. The thick black curves show the radial location of the maximum azimuthally averaged tangential wind speed as a function of height.

30 and 140 km radius, with maximum ascent exceeding 0.4 m s^{-1} centred at a radius of about 65 km in the height range 8−10 km.

To begin, we examine the tangential wind tendency in (i), which is the sum of the tendency terms shown in (c)−(h). This tendency is positive in a broad region stretching from near the axis to a radius of at least 100 km, a region that straddles the RMW. The tendency is negative close to the surface, in the upper troposphere (above about 13 km, except in two small localized radial bands) and in a prominent region in an annulus from 20 to

40 km radius above about 6.5 km. The latter feature, together with the strong positive tendency at smaller radii, is clearly associated with the eddy contribution (f).

To understand the structure of the tendency in Figure 11(i), we first examine the contributions from the mean advection terms in (c) and (d). These terms are associated with the import of mean cyclonic absolute vorticity in the boundary layer and the lofting of enhanced tangential momentum by the aggregate of deep cumulus convection into the vortex interior, respectively. The
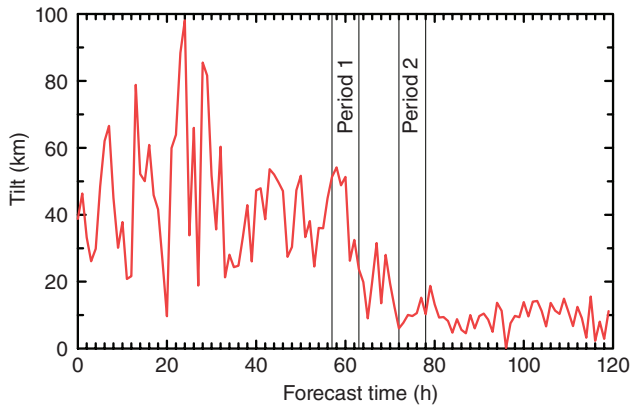
Figure 12. Plot of vortex tilt (km) from 1 to 8 km altitude for the 5 day HWRF forecast of Hurricane *Earl* (2010). The vortex centre at each level is defined as the location with the minimum horizontal wind speed. The two averaging periods, 57–63 and 72–78 h, referred to in the text are indicated by thin vertical lines.

large positive tendency below about 1.5 km in (c) is a reflection of the boundary-layer import of absolute vorticity, but there is strong cancellation between this effect and the subgrid-scale vertical diffusion resulting from surface friction (h). Nevertheless, there is a positive spin-up tendency of the tangential wind in the boundary layer (see (i)), which is, in essence, a manifestation of the boundary-layer spin-up mechanism. The contribution to the spin-up tendency from the mean boundary-layer inflow corroborates that of Bui *et al.* (2009, their figure 9, panels (a), (c) and (e)) and Persing *et al.* (2013).

In Figure 11(c), there is a very shallow layer of negative mean radial vorticity influx near 1 km height and between approximately 10 and 40 km radius. The negative tendency is associated with the outward motion of air parcels after they have emerged from the boundary layer and it is partially cancelled out by the vertical advection of enhanced mean tangential velocity emerging from the boundary layer (Figure 11(d)). This negative mean radial vorticity flux feature is, in part, a consequence of the boundary-layer spin-up mechanism discussed above and is seen as a localized positive tangential wind tendency below 1 km in altitude and beyond a radius of about 20 km in Figure 11(i). In a similar way, the negative tendency between 7 and 12 km in the mean radial vorticity influx (Figure 11(c)) is largely cancelled out by the vertical advection of mean tangential velocity (Figure 11(d) and (e)). The latter feature is a reflection of the upward and outward movement of moist air parcels.

In summary, the mean dynamics are similar to those that operate in a quiescent environment, as described in Persing *et al.* (2013), even though the latter study did not include a representation of ice microphysics.

The contribution to the tangential wind tendency from the eddy terms is shown in Figure 11(f). It is evident that the eddy contributions are at least comparable in magnitude with the mean tendency terms and, as noted above, there are some prominent regions inside the RMW where they are even dominant.

At low levels, the combined eddy tendency[††] suggests a weakening of the maximum tangential wind and a strengthening of the tangential winds inside the RMW. While it might be tempting to attribute this weakening/strengthening signature to a diffusive mixing process by the eddies, caution is advised for

---

[††]It turns out that structure of the eddy tendency terms is dominated by the horizontal eddy vorticity flux term for the RI intervals analyzed (not shown). Nevertheless, the structure of the eddy vertical advection of tangential momentum is found to be consistent with that reported in Persing *et al.* (2013) and is positive through the troposphere around the eyewall region, with a maximum in the middle to upper troposphere. This term is associated with the vortical plume activity that has been discussed elsewhere in Montgomery and Smith (2014 and references therein). This positive spin-up effect has been noted also by Krishnamurti (2015, personal communication) under the name of 'cumulus torque'.

reasons discussed in Persing *et al.* (2013) (see also McIntyre, 1993a, b). A comparison of Figure 11(f) with Figure 11(g) shows clearly a very different spin-up structure near and inside the RMW between the eddy tendency and the diffusive tendency, indicating that the resolved eddy tendencies cannot be interpreted as a mixing process down the mean angular velocity gradient. As foreshadowed in section 5, the convectively generated cyclonic vorticity anomalies (Figure 6, left column) exhibit a tendency to axisymmetrize inside the RMW. The tendency for these disturbances to be axisymmetrized can be anticipated by the significant departure from solid-body rotation inside the RMW, as suggested in Figure 6.

At mid to upper levels, the combined eddy tendency indicates a significant spin-up in a region straddling the RMW. Given the fact that the incipient storm was intensifying in the presence of a moderately strong northeasterly vertical shear (see Figure 2), this eddy spin-up signature may be, in part, a reflection of the alignment of the intensifying storm in the presence of vertical shear, as it is not found in Persing *et al.* (2013, cf. their figure 10(g)), nor during the second intensification period when the vortex tilt has become significantly reduced (see their figure 13(f) and accompanying discussion). The alignment of the storm itself is evidenced by Figure 12, which shows clearly the reduction of the tilt between 1 and 8 km altitude. The dynamics underlying this tilt reduction comprise a topic requiring further investigation.

Figure 11(j) shows a direct estimate of the total tangential wind tendency over the period 57–63 h from a difference in $\langle v \rangle$ over this interval. This tendency should be compared with the estimate from the sum of tendency terms shown in Figure 11(i). While the direct estimate is much smoother and somewhat smaller in magnitude, it does show a sloping band of strong tendency, largely inside the RMW. The difference between the two estimates is to be expected, because the estimate from sum of terms reflects variability associated with deep convection between individual hourly times in the 57–63 h average (not shown). This variability is dominated inside the RMW by the eddy terms.

7.4.2. Period 2

Figure 13 shows the time-averaged fields equivalent to those in Figure 11, but for the mature phase of *Earl*'s rapid intensification (Period 2 in Figure 3). By this time, the tangential wind field has strengthened and contracted (compare Figure 13(a) with Figure 11(a)), as has the secondary circulation (Figure 13(b)). In particular, the main region of ascent has narrowed and the maximum mean vertical velocity has increased (compare Figure 13(b) with Figure 11b).

All subsequent panels exhibit a radial contraction of the tendency contributions shown in Figure 11. This contraction is presumably associated with the focusing and organization of deep convection as the storm matures. In contrast to Figure 11, the appreciable net spin-up of tangential velocity is confined to below about 10 km height and is mainly inside the RMW (Figure 13(i)). There is significant cancellation of the individual tendencies in the upper troposphere, a feature that reflects, in part, the approximate material conservation of M, but it is evident that a large spin-down tendency associated with eddy effects (Figure 13(f)) has an important contribution to this cancellation.

The most prominent features in Figure 13(c) are the positive spin-up tendency in the boundary layer out to a radius of more than 150 km and the elevated feature between about 2 and 5 km in height that straddles the RMW. With respect to the former, there is a large, but not exact, cancellation between the mean radial advection of vorticity $V_{m\zeta}$ (Figure 13(c)) and the vertical diffusion V_{dv} (Figure 13(h)); the positive tendency in dV/dt (Figure 13(i)) indicates that the boundary-layer spin-up mechanism is still operative and contributes to a spin-up of the eyewall (Schmidt and Smith, 2016). With respect to the latter, the elevated feature
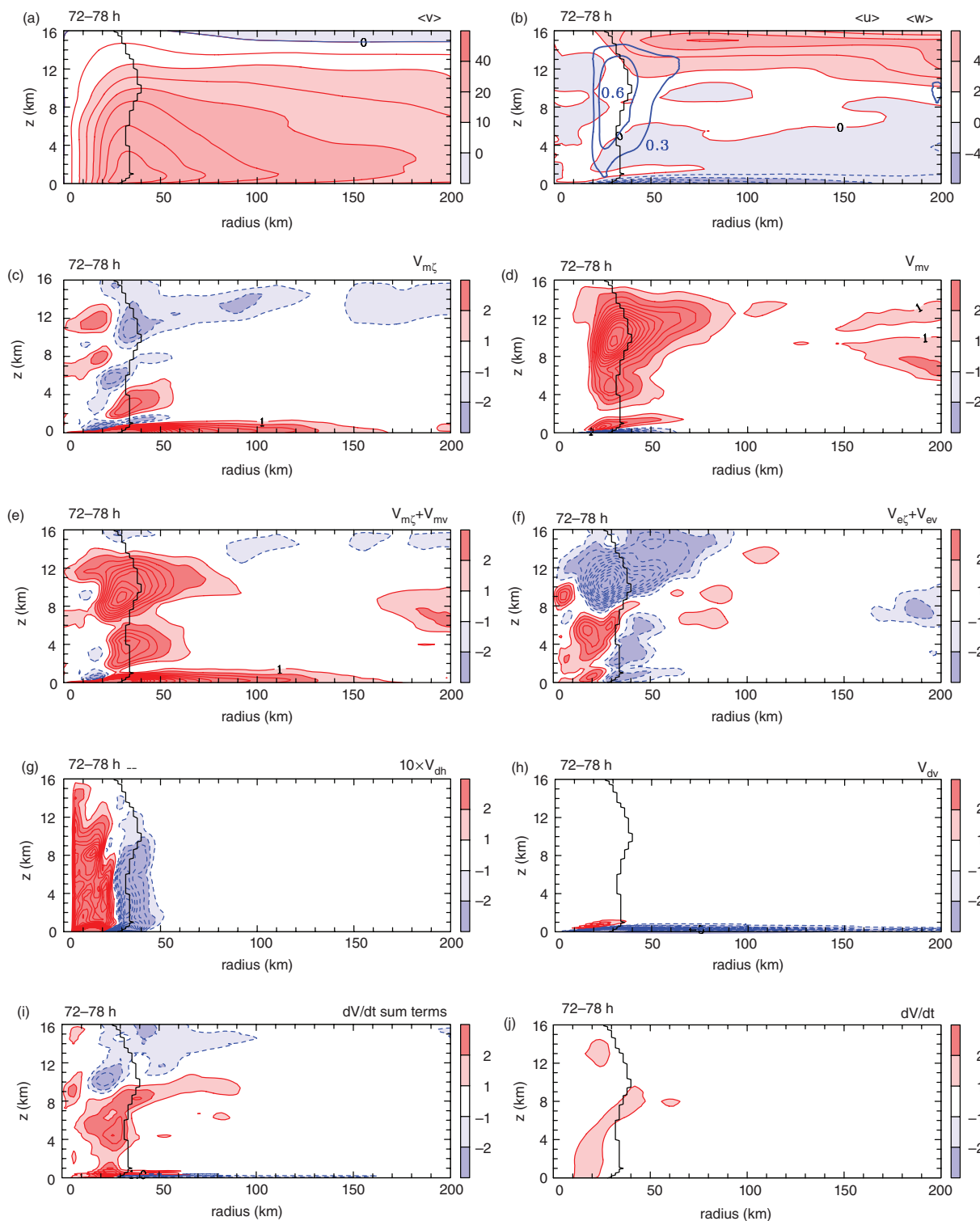
Figure 13. Legend as for Figure 11, but for the period 72–78 h. Also, the contour interval for the tendencies has been doubled to 1 m s^{-1} h^{-1}. The shading intervals are as indicated on the side bar in units of m s^{-1} h^{-1}.
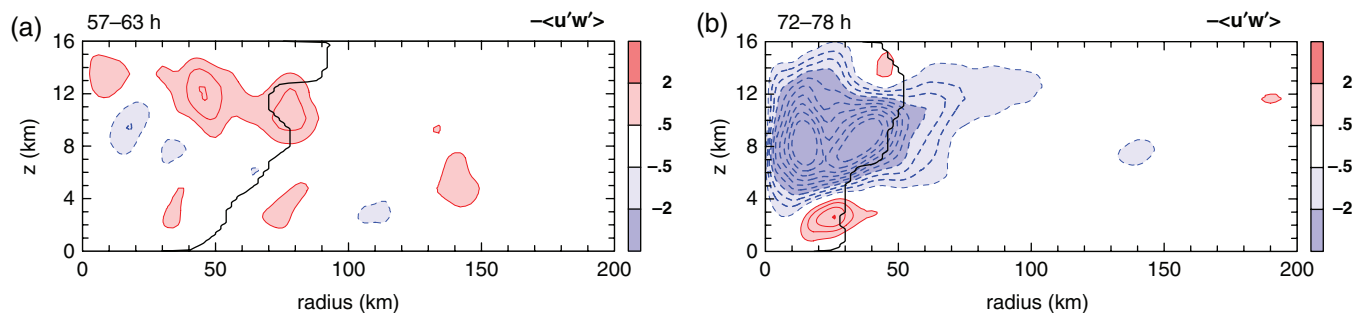

Figure 14. Eddy covariance field $< -u'w' >$ associated with the vertical eddy flux of eddy radial momentum in Eq. (5) averaged during the time periods (a) 57–63 h and (b) 72–78 h. Contour interval: 0.5 m^2 s^{-2}. Colour shading is as indicated in the side bar in units of m^2 s^{-2}.

between 2 and 5 km is a manifestation of the centrifugal recoil effect, as rapidly swirling supergradient air exits the boundary layer and adjusts towards a state of near gradient wind balance (see Persing *et al.*, 2013, p. 12319). This recoil effect contributes to spinning up the eyewall, as seen in the sum of the mean advection terms (Figure 13(e)).

The principal features in Figure 13(d) reflect the lofting of enhanced tangential momentum at the top of the boundary layer generated by the boundary-layer spin-up mechanism. When interpreting this panel (and indeed Figure 11(d)), it is important to recall that there is a certain projection of localized deep convective momentum transport into the azimuthally averaged flow.

Since the combined eddy tendency shown in Figure 13(f) is dominated by the horizontal eddy vorticity flux term, the positive and negative horizontal dipole structure below about 7.5 km centred around the time-evolving RMW is consistent with supporting the contraction of the RMW evident in Figure 8. As in Figure 11, the positive horizontal diffusive tendency is largest well inside the RMW (Figure 13(g)) and the negative diffusive tendency acts in opposition to the positive eddy contribution near the RMW in the mid-troposphere (Figure 13(f)). Note the large spin-down tendency of the eddies in the upper troposphere, which has no analogue in the subgrid-scale tendency. Moreover, as in Period 1, the subgrid-scale tendency is an order of magnitude smaller than the other tendencies.

As found in Period 1, there are differences between the tendency calculated as a sum of terms (Figure 13(i)) and that diagnosed directly from the model output (Figure 13(j)). While the pattern of spin-up is similar in the two panels, the directly calculated tendency is again weaker than that calculated as a sum of tendency terms.

7.4.3. Vertical flux of eddy radial momentum

Figure 14 shows the eddy covariance field $\langle -u'w' \rangle$ associated with the vertical eddy flux of eddy radial momentum. The sign convention is as defined in Persing *et al.* (2013), so as to yield an effective force per unit mass if the material form of the radial momentum equation (5) were written in flux form, with eddy covariance terms placed on the right-hand side of the equation. The vertical derivative of this term is linked to the term labelled U_{ev} in Eq. (5). In Persing *et al.* (2013), this eddy term was shown to exhibit a negative pattern spanning the deep troposphere. The vertical divergence of this term was shown to contribute to an enhanced overturning circulation during the intensification process, with a tendency to enhance inflow at low levels and enhance outflow at upper levels associated with the vortical plume structures in the zone of deep cumulus convection near and around the developing eyewall. This eddy effect is a distinctly agradient effect and one that is not represented in the (conventional) classical spin-up model described at leading order by axisymmetric balance dynamics (e.g. Shapiro and Willoughby, 1982).

The first panel of Figure 14 shows only a weak incoherent signature of this eddy covariance field during the initial spin-up of the storm (Period 1 in Figure 3). The second panel of Figure 14, which applies to Period 2 in Figure 3, shows a coherent negative pattern in the eddy covariance field near and inside the radius of maximum tangential wind. During this later period, the negative eddy momentum flux is such as to contribute to an enhanced inflow in the lower troposphere (above about 2 km) and an enhanced outflow in the upper troposphere (above about 9 km), broadly consistent with the results found in Persing *et al.* (2013) in the absence of ambient vertical shear. The other two eddy covariance terms $\langle -u'v' \rangle$ and $\langle -v'w' \rangle$ are not shown, because the material analogue of these terms has been shown in Figure 10 in association with the terms $V_{e\zeta}$ and V_{ev}, respectively.

For completeness, to complement our analysis of the mean agradient force (U_{magf}) shown in Figure 9, we computed the eddy

agradient force (U_{eagf}) in Eq. (5). However, this term is generally a small fraction of the mean term and is not shown.

7.4.4. More on the role of eddy processes

As noted above, the mean dynamics of vortex intensification in vertical shear are similar to those that operate for a vortex in a quiescent environment, but the effects of shear introduce additional contributions to the eddy momentum dynamics. We have shown that the eddy processes in the presence of vertical shear make an important contribution to spin-up of the winds at and inside the RMW during phases of rapid intensification. The eddy processes cannot be ignored in a complete fluid dynamical interpretation of the intensification process. The eddies are mainly a reflection of the transient effects of localized deep convection in the broader-scale vortex circulation, which is itself affected by the shear.

As noted above, one effect of shear is to tilt the vortex and, even in the absence of deep convection, the tilt will excite vortex Rossby waves. These waves can lead to a reduction of the tilt (Reasor and Montgomery, 2015; Schecter, 2015), as can the vertical momentum transport by deep convection within the vortex core. A more complete understanding of the dynamics underlying this tilt reduction would be of practical and theoretical interest. In particular, it is not yet known whether the tilt reduction of this storm during the spin-up process is the result of a damped vortex Rossby-wave core mode (Reasor and Montgomery, 2015), the consolidation of convectively generated vorticity anomalies into an erect vorticity monolith during the vertical shear interaction (Reasor and Montgomery, 2001) or convectively induced eddy momentum convergence. A resolution of these issues requires an analysis of the asymmetries themselves and the possible coherent vortex Rossby-wave envelope, as in (Riemer *et al.*, 2010). This interesting topic lies outside the scope of the current investigation.

8. Conclusions

The present study was motivated by the desire to understand better the intensification of Atlantic Hurricane *Earl* (2010), which was particularly well-documented by aircraft observations. We have used a high-resolution numerical simulation of this storm to examine the dynamics and thermodynamics of its intensification in relatively strong vertical shear in the context of a recent paradigm for tropical cyclone intensification. We showed that the simulation, which uses the NOAA−HWRF state-of-the-art forecast model, adequately captures the track, intensification and azimuthally averaged structure of the observed storm during the period of rapid intensification. On these grounds, it serves as a useful laboratory for appraising elements of the new paradigm. In particular, the present work studies both the system scale and local eddy dynamics of the intensification process.

Consistent with recent observational work, we find that the spin-up of the tangential wind field above the boundary layer occurs as the absolute angular momentum surfaces are drawn inwards by the aggregate heating of the rotating convective clouds in the interior of the vortex. This is the so-called 'classical spin-up mechanism' at work. However, the maximum tangential wind is found to lie within the boundary layer, a feature that is not part of the latter mechanism. The large wind speeds in the boundary layer are significantly supergradient in both the simulation and observations of *Earl*. These supergradient winds are an important element of the spin-up of the inner-core region of the vortex, as they act to arrest the boundary layer inflow and thereby influence where the air ascends into the eyewall updraught. The foregoing findings support the new paradigm of tropical cyclone intensification on the system scale.

The presence of vertical shear during *Earl*'s rapid intensification introduces eddy processes in addition to the intrinsic eddy processes found previously in a quiescent environment associated

© 2016 The Authors. *Quarterly Journal of the Royal Meteorological Society* published by John Wiley & Sons Ltd on behalf of the Royal Meteorological Society.

Q. J. R. Meteorol. Soc. **143**: 293–308 (2017)

with vortical plume structures in and around the developing eyewall region. Non-axisymmetric aspects of the intensification process have been studied using a diagnostic analysis of the horizontal momentum equations, including both mean and eddy components in the azimuthally averaged equations for radial and tangential momentum. Despite the detrimental influence of the shear on the vortex alignment and on depressing the pseudo-equivalent potential temperature outside the developing eyewall, the combined eddy processes associated with the vortical plume structures in and around the developing eyewall region are shown to contribute significantly to an intensifying storm and an enhanced overturning circulation. These eddy processes are distinctly agradient effects that are not features of the classical spin-up mechanism.

In summary, we have shown that the new paradigm for tropical cyclone intensification is useful in understanding the physics of intensification in the presence of vertical shear. In terms of the azimuthal mean dynamics, the effects of deep convection and vertical shear are manifest as eddy terms in the governing equations. Here we have quantified the main eddy terms in the two horizontal momentum equations during the intensification of Hurricane *Earl*.

The availability of model output at one-hourly intervals was found to impose some limitations in calculating the time mean of eddy processes associated with deep convection. In future studies, much more frequent output would be desirable. At this stage, it would be enlightening to carry out a more idealized study of intensification in vertical shear, applying the same methodology as described here with output at much more frequent time intervals. For example, it remains to be understood how the rotating convective updraughts combine to produce the diagnosed structures of the eddy terms themselves and how vortex Rossby waves and other eddies contribute to the alignment of the vortex during intensification.

Acknowledgements

References

Bolton D. 1980. The computation of equivalent potential temperature. *Mon. Weather Rev.* **108**: 1046–1053.

Bui HH, Smith RK, Montgomery MT, Peng J. 2009. Balanced and unbalanced aspects of tropical-cyclone intensification. *Q. J. R. Meteorol. Soc.* **135**: 1715–1731.

Carrier GF. 1971. Swirling flow boundary layers. *J. Fluid Mech.* **49**: 133–144.

Carrier GF, Hammond AL, George OD. 1971. A model of the mature hurricane. *J. Fluid Mech.* **47**: 145–170.

Charney JG, Eliassen A. 1964. On the growth of the hurricane depression. *J. Atmos. Sci.* **21**: 68–75.

Chen S, Gopalakrishnan S. 2015. A study on the asymmetric rapid intensification of Hurricane *Earl* (2010) using the HWRF system. *J. Atmos. Sci.* **72**: 531–550.

Chen Y, Yau MK. 2001. Spiral bands in a simulated hurricane. Part I: Vortex Rossby wave verification. *J. Atmos. Sci.* **58**: 2128–2145.

Chen Y, Brunet G, Yau MK. 2003. Spiral bands in a simulated hurricane. Part II: wave activity diagnostics. *J. Atmos. Sci.* **60**: 1239–1256.

DeMaria M, Mainelli M, Shay LK, Knaff JA, Kaplan J. 2005. Further improvements to the Statistical Hurricane Intensity Prediction Scheme (SHIPS). *Weather and Forecasting* **20**: 531–543.

Enagonio J, Montgomery MT. 2001. Tropical cyclogenesis via convectively forced vortex Rossby waves in a shallow water primitive equation model. *J. Atmos. Sci.* **57**: 685–706.

Ferrier BS. 1994. A double-moment multiple-phase four-class bulk ice scheme. Part I: Description. *J. Atmos. Sci.* **51**: 249–280.

Franklin JL, Lord SJ, Feuer SE, Marks FD. 1993. The kinematic structure of Hurricane Gloria (1985) determined from nested analyses of dropwindsonde and Doppler radar data. *Mon. Weather Rev.* **121**: 2433–2451.

Gall R, Franklin J, Marks F, Rappaport EN, Toepfer F. 2013. The Hurricane Forecast Improvement Project. *Bull. Am. Meteorol. Soc.* **94**: 329–343.

Gopalakrishnan SG, Marks F, Zhang X, Bao J-W, Yeh K-S, Atlas R. 2011. The experimental HWRF System: A study on the influence of horizontal resolution on the structure and intensity changes in tropical cyclones using an idealized framework. *Mon. Weather Rev.* **139**: 1762–1784.

Gopalakrishnan SG, Marks F, Zhang JA, Zhang X, Bao J-W, Tallapragada V. 2015. A study of the impacts of vertical diffusion on the structure and intensity of the tropical cyclones using the high-resolution HWRF system. *J. Atmos. Sci.* **70**: 524–541.

Hong S-Y, Pan HL. 1996. Nonlocal boundary layer diffusion in a medium-range forecast model. *Mon. Weather Rev.* **124**: 2322–2339.

Jones SC. 1995. The evolution of vortices in vertical shear. I: Initially barotropic vortices. *Q. J. R. Meteorol. Soc.* **121**: 821–851.

Kepert JD. 2012. Choosing a boundary-layer parametrization for tropical cyclone modelling. *Mon. Weather Rev.* **140**: 1427–1445.

Kilroy G, Smith RK. 2016. Tropical-cyclone convection: the effects of a near tropical storm strength vortex on deep convection. *Q. J. R. Meteorol. Soc.* **140**. In Press.

Kilroy G, Smith RK, Montgomery MT. 2015. Why do model tropical cyclones grow progressively in size and decay in intensity after reaching maturity? *J. Atmos. Sci.* **73**: 487–503.

McIntyre ME. 1993a. Isentropic distributions of potential vorticity and their relevance to tropical cyclone dynamics. In *Proceedings of ICSU/WMO International Symposium on Tropical Cyclone Disasters*, Lighthill J, Zheng Z, Holland G, Emanuel K. (eds.): 143–156. Peking University Press: Beijing, China.

McIntyre ME. 1993b. Atmospheric dynamics: some fundamentals, with observational implications. In *The use of EOS for Studies of Atmospheric Physics, Proceedings of the International School of Physics Enrico Fermi*, CXV Course, Gille JC, Visconti G. (eds.): 313–386. North Holland, Amsterdam, The Netherlands.

McWilliams JC, Graves LP, Montgomery MT. 2003. A formal theory for vortex Rossby waves and vortex evolution. *Geophys. Astrophys. Fluid Dyn.* **97**: 275–309.

Melander MV, McWilliams JC, Zabusky NJ. 1987. Axisymmetrization and vorticity-gradient intensification of an isolated two-dimensional vortex through filamentation. *J. Fluid Mech.* **178**: 137–159.

Montgomery MT, Enagonio J, 1998. Tropical cyclogenesis via convectively forced vortex Rossby waves in a three-dimensional quasigeostrophic model. *J. Atmos. Sci.* **55**: 3176–3207.

Montgomery MT, Smith RK, 2014. Paradigms for tropical-cyclone intensification. *Aust. Meteorol. Oceanogr. J.* **64**: 37–66.

Montgomery MT, Nicholls ME, Cram TA, Saunders AB. 2006. A vortical hot tower route to tropical cyclogenesis. *J. Atmos. Sci.* **63**: 355–386.

Montgomery MT, Nguyen SV, Smith RK, Persing J. 2009. Do tropical cyclones intensify by WISHE? *Q. J. R. Meteorol. Soc.* **135**: 1697–1714.

Montgomery MT, Zhang J, Smith RK. 2014. An analysis of the observed low-level structure of rapidly intensifying and mature hurricane *Earl* (2010). *Q. J. R. Meteorol. Soc.* **140**: 2132–2146.

Montgomery MT, Persing J, Smith RK. 2015. Putting to rest WISHE-ful misconceptions. *J. Adv. Model. Earth Syst.* **7**: 92–109, doi: 10.1002/2014MS000362.

Nguyen SV, Smith RK, Montgomery MT. 2008. Tropical-cyclone intensification and predictability in three dimensions. *Q. J. R. Meteorol. Soc.* **134**: 563–582.

Nolan DS, McGauley MG. 2012. Tropical cyclogenesis in wind shear: Climatological relationships and physical processes. In *Cyclones: Formation, Triggers and Control*, Oouchi K, Fudeyasu H. (eds.): 1–36. Nova Science Publishers, Happauge, NY.

Ooyama KV. 1969. Numerical simulation of the life cycle of tropical cyclones. *J. Atmos. Sci* **26**: 3–40.

Ooyama KV. 1982. Conceptual evolution of the theory and modeling of the tropical cyclone. *J. Meteorol. Soc. Jpn* **60**: 369–380.

Persing J, Montgomery MT, McWilliams J, Smith RK. 2013. Asymmetric and axisymmetric dynamics of tropical cyclones. *Atmos. Chem. Phys.* **13**: 12299–12341.

Reasor PD, Montgomery MT. 2001. Three-dimensional alignment and co-rotation of weak, TC-like vortices via linear vortex Rossby waves. *J. Atmos. Sci.* **58**: 2306–2330.

Reasor PD, Montgomery MT. 2015. Evaluation of a heuristic model for tropical cyclone resilience. *J. Atmos. Sci.* **72**: 1765–1782.

Reasor PD, Montgomery MT, Grasso LD. 2004. A new look at the problem of tropical cyclones in vertical shear flow: vortex resiliency. *J. Atmos. Sci.* **61**: 3–22.

Riemer M, Montgomery MT. 2011. Simple kinematic models for the environmental interaction of tropical cyclones in vertical wind shear. *Atmos. Chem. Phys.* **11**: 9395–9414.

Riemer M, Montgomery MT, Nicholls ME. 2010. A new paradigm for intensity modification of tropical cyclones: Thermodynamic impact of vertical wind shear on the inflow layer. *Atmos. Chem. Phys.* **10**: 3163–3188.

Riemer M, Montgomery MT, Nicholls ME. 2013. Further examination of the thermodynamic modification of the inflow layer of tropical cyclones by vertical wind shear. *Atmos. Chem. Phys.* **13**: 327–346.

Rogers RF, Reasor PD, Zhang JA. 2015. Multiscale structure and evolution of Hurricane *Earl* (2010) during rapid intensification. *Mon. Weather Rev.* **143**: 536–562.

Rotunno R, Emanuel KA. 1987. An air–sea interaction theory for tropical cyclones. Part II: evolutionary study using a nonhydrostatic axisymmetric numerical model. *J. Atmos. Sci.* **44**: 542–561.

Sanger NT, Montgomery MT, Smith RK, Bell MM. 2012. An observational study of tropical-cyclone spin-up in Supertyphoon *Jangmi* (2008) from 24–27 September. *Mon. Weather Rev.* **142**: 3–28.

Schecter DA. 2015. Response of a simulated hurricane to misalignment forcing compared to the predictions of a simple theory. *J. Atmos. Sci.* **72**: 1235–1260.

Schmidt C, Smith RK. 2016. Tropical cyclone evolution in a minimal axisymmetric model revisited. *Q. J. R. Meteorol. Soc.* **142**: 1505–1516.

Shapiro LJ, Montgomery MT. 1993. A three-dimensional balance theory for rapidly rotating vortices. *J. Atmos. Sci.* **50**: 3322–3335.

Shapiro LJ, Willoughby H. 1982. The response of balanced hurricanes to local sources of heat and momentum. *J. Atmos. Sci.* **39**: 378–394.

Smith RK. 1968. The surface boundary layer of a hurricane. *Tellus* **20**: 473–484.

Smith RK, Montgomery MT. 2010. Hurricane boundary-layer theory. *Q. J. R. Meteorol. Soc.* **136**: 1665–1670.

Smith RK, Montgomery MT. 2015. Towards clarity on tropical cyclone intensification. *J. Atmos. Sci.* **72**: 3020–3031.

Smith RK, Ulrich W, Dietachmayer G. 1990. A numerical study of tropical cyclone motion using a barotropic model. Part I. The role of vortex asymmetries. *Q. J. R. Meteorol. Soc.* **116**: 337–362.

Smith RK, Montgomery MT, Nguyen SV. 2009. Tropical-cyclone spin-up revisited. *Q. J. R. Meteorol. Soc.* **135**: 1321–1335.

Tallapragada V, Kieu C, Kwon Y, Trahan S, Liu Q, Zhang Z, Kwon I-H. 2014. Evaluation of storm structure from the operational HWRF during 2012 implementation. *Mon. Weather Rev.* **142**: 4308–4325.

Yablonsky RM, Ginis I. 2008. Improving the ocean initialization of coupled hurricane-ocean models using feature-based data assimilation. *Mon. Weather Rev.* **136**: 2592–2607.

Yang B, Wang Y, Wang B. 2007. The effect of internally generated inner-core asymmetrics on tropical cyclone potential intensity. *J. Atmos. Sci.* **64**: 1165–1188.

Zhang JA, Rogers RF, Nolan DS, Marks FD. 2011a. On the characteristic height scales of the hurricane boundary layer. *Mon. Weather Rev.* **139**: 2523–2535.

Zhang JA, Marks FD, Montgomery MT, Lorsolo L. 2011b. An estimation of turbulent characteristics in the low-level region of intense Hurricanes *Allen* (1980) and *Hugo* (1989). *Mon. Weather Rev.* **139**: 1447–1462.

Zhang JA, Gopalakrishnan SG, Marks FD, Rogers RF, Tallapragada V. 2012. A developmental framework for improving hurricane model physical parameterization using aircraft observations. *Trop. Cycl. Res. Rev.* **1**: 419–429.

Zhang JA, Nolan DS, Rogers RF, Tallapragada V. 2015. Evaluating the impact of improvements in the boundary layer parameterization on hurricane intensity and structure forecasts in HWRF. *Mon. Weather Rev.* **143**: 3136–3155.